Plasma jets and narrow bandwidth ion spectra from thin foils irradiated at high laser intensity

K. Kakolee, S. Kar, D Doria,B. Ramakrishna, G. Sarri, K. Quinn, M. Borghesi

School of Mathematics and Physics, Queen's University of Belfast, Belfast, BT7 1NN, U. K

J. Osterholz, M. Cerchez, O. Willi,

Heinrich Heine-Universitat Dusseldorf, Germany.

X. Yuan, P. McKenna

SUPA, Department of Physics, University of Strathclyde, Glasgow, UK.

Abstract:

Evolution of collimated plasma jets and ion acceleration from micron to sub-micron thickness foils following the interaction of ultra intense (up to 3 $\times 10^{20}$ W/cm^2) laser pulses is investigated. We characterized the correlation between laser intensity and target areal density for the formation of a supersonic dense plasma jet. With the maximum achievable intensity on target, jets with Mach number up to 10 have been observed from few microns thick Cu foils expanding longitudinally with a speed of 2×10^6 m/s. With circular polarization, the uniformity of jet density profile has improved significantly as compared to the jets observed from interaction of a linearly polarized laser. While the moderate energy (KeV) overdense plasma jets are formed efficiently for micron thickness target irradiated at 10^{20} W/cm^2 intensity, decreasing the target areal density or increasing irradiance on target leads to so-called light-sail RPA [1] regime in which the ions, independent of their charge to mass ratio, are accelerated to tens of MeV/nucleon energies.

Introduction: One of the main applications of high power lasers is to simulate various astrophysical phenomena in laboratories. Jets and collimated outflows are omnipresent in the universe associated with the formation of young stars, planetary nebulae, X-ray binaries and active galactic nuclei (AGNs) [2]. Although the experimental jets driven by high power lasers are of much smaller scales compared to stellar or extragalactic objects, they may provide an excellent opportunity to study in the laboratory the underlying mechanisms.

In laboratory experiments, plasma jets relevant to astrophysics have been generated typically by employing nsec long laser pulses of hundreds of joules energy [3-5]. In this Letter, we have characterised the conditions for the formation of supersonic jets driven by pico-second laser pulses of similar energies, as observed previously by Kar et. al [6]. At such high irradiance (around 10^{20} W/cm^2), jets can be produced by the strong ponderomotive pressure exerted on thin targets by the laser. Via parametric scans (laser intensity, target areal density) we have identified the suitable conditions for the formation of a sustained supersonic jet. The temporal evolution of the jets up to ns time is studied by time resolved optical interferometry. Apparently, beyond the parameter ranges required for sustained plasma jet, strong modulation in MeV proton/ion spectra is observed as we increase the laser irradiance or decrease the target areal density. Preliminary analysis of the ion spectra will be discussed.

Experiment:

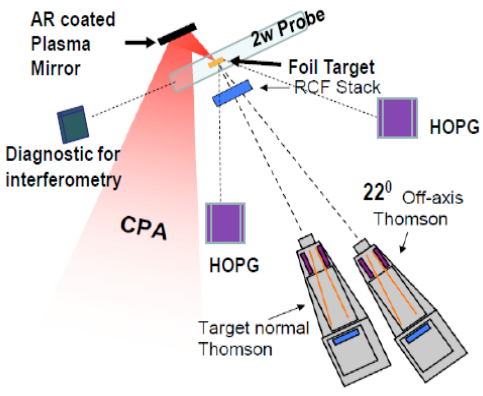

Fig 1. Schematic of the experimental set up.

The experiment was carried out in the Vulcan Nd: glass laser of Rutherford Appleton Laboratory, U.K., operating in chirped pulse amplification (CPA) mode. An f=4.5 (f=3) off-axis parabola was used to focus the laser down to a 10 µm full width at half maximum (FWHM) spot, attaining peak intensity of 3×10^{20} W/cm^2 on the target. A plasma mirror was used in order to suppress the intensity of amplified spontaneous emission and prepulses. The laser was irradiating the target at nearly 0 degree incidence angle. The polarisation of the laser on target was varied by using a quarter wave plate. The intensity on the target was varied, as required by the interaction intensity scans, by increasing the laser spot size on the target by translating the parabola along the focussing axis. Targets of various materials and thicknesses (free standing thin foils, 10 µm to 100 nm) were used in this experiment. The plasma outflow from the target was probed by employing a transverse Nomarsky interferometer [7] and shadowgraphy with high spatial (few microns) and temporal (ps) resolution. Figure 1 shows a schematic of the experimental arrangement. The probe beam was frequency doubled from a portion of the main CPA pulse to a wavelength 527 nm. The converted beam was splitted into two parts and projected onto the target, transverse to the interaction axis, from two different angles. The time of arrival of each beam on the target was controlled separately by delaying their path length. The setup was designed to achieve two ps snapshots of the interaction at different times in a single shot. The interferograms were recorded by 12 bit dynamic range CCD cameras. The plasma electron density profile from the interferogram was reconstructed by retrieving the phase map using fast Fourier transform of the fringe pattern in the interfeogram, followed by Abel inversion of the phase map assuming a cylindrical symmetry [8].

The main diagnostic for multi Mev proton emission was Thomson Parabola Spectrometer (TP –Spec). Two high resolutions TP –Spec were fielded, one along the target normal direction and the other looking at 22^0 off axis to the target normal. Image plates (IP) were used to record the ion spectra. By using differential filtering the response of the image plate to different energy ions was calibrated which will be discussed in another report.

Result and Discussions: The temporal evolution of the collimated plasma jets at the target rear side was observed from 150 ps to 1.1 ns, after the arrival of the CPA on the target, over many shots. 1 µm thick Cu foil was used for this temporal scan and the laser intensity on target was kept at its maximum (2-3$\times10^{20}$ W/cm^2). The plasma jets maintained their degree of collimation over ns time scales as shown in the fig. 2(a). From the temporal scan, the transverse and longitudinal dimensions of the jets were inferred at different probing time, as shown in the Fig. 2(b). Over this probing time period, the results suggest a non-linear (a power law) time dependent velocity for the longitudinal expansion of the jets, whereas an almost constant expansion velocity is observed for the transverse direction. Consequently, the Mach number of the jets, estimated as a ratio between the longitudinal to transverse velocities, has a strong time dependence during the first few hundreds of ps after the interaction.

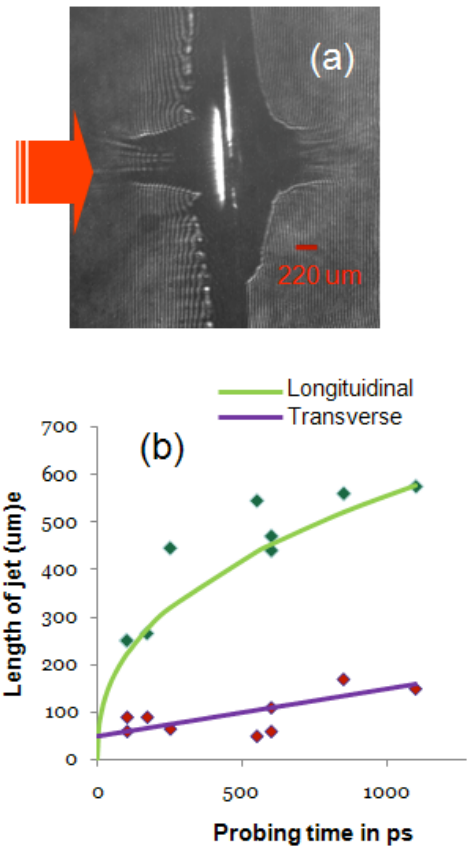

Fig 2. (a) Plasma jet at 850 ps after the interaction with 1 µm Cu target. (b) Temporal evolution of the plasma jets produced from 1 um thick Cu target irradiated at 2-3x10^{20} W/cm^2.

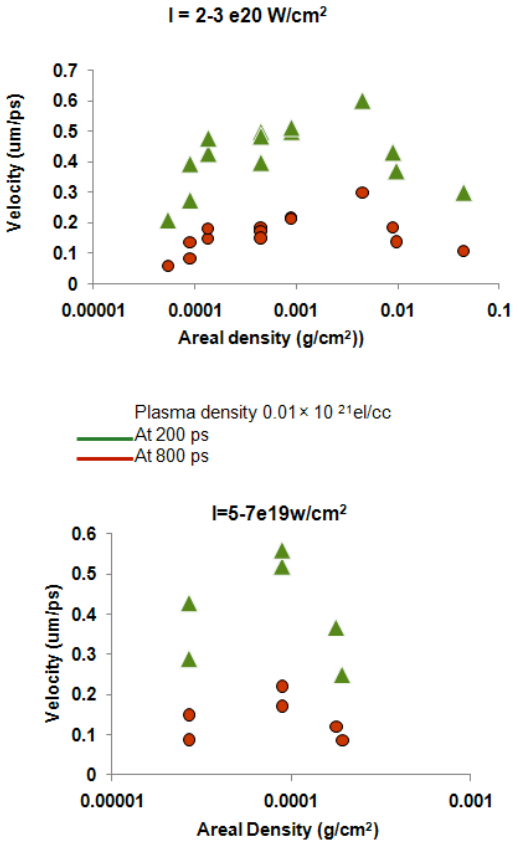

Fig 3(a) and (b). Velocity of jet for different target areal densities (at given laser intensity)

In order to parametrise the underlying mechanism behind the collimated jet formation, scans were made observing the rear side plasma jets at different laser intensity for same target and at same intensity for different target areal density (thickness x density). For a given laser intensity, the jet velocity increases as we decrease the areal density (moving to thinner targets or lower Z targets) and attains maximum at a certain value of areal density. As we decrease the areal density further, the jet velocity drops sharply. In fact for the lower areal density targets the interferograms shows plasma density profiles, which one would expect from a blow-off target. However in this regime, the ion spectrum shows features which suggest the onset of the so called light sail radiation pressure acceleration mechanism [1], which will be discussed later. A similar trend of jet velocity variation with areal density is observed for two different laser intensities and the areal density for which the jet velocity is maximum is lower, as expected, for lower irradiance [see fig 3(a) and (b)]. This behavious is also observed for circular polarisation of the interaction laser. As shown in the Fig, 4(b) a sustained high mach number plasma jet from thinner targets can be produced by lowering the laser intensity commensurately. For example, a factor of 10 less intense laser produces jet of similar mach number from 100 nm target than that required in case of 1 um thick target.

However, there is a distinct difference between the plasma jets produced from a laser at linearly polarised to circularly polarised. It can be seen pedagogically by comparing the raw images of the jets shown in Fig. 2(a) and 4(a) that the plasma front of the jets in case of circular polarisaiton (Fig. 4(a)) is flat and uncorrupted as compared to the one in linear polarisation (Fig. 2(a)).

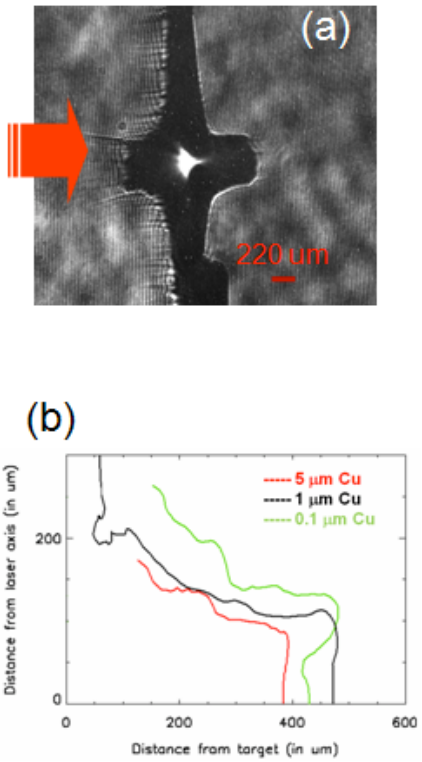

Fig 4(a) Plasma jet at 600 ps after the interaction with 1 µm Cu target at circular polarisation of laser. (b) Thickness scan for 1 um target at circular polarisation of laser for the density of 10^{19} el/cc, for 0.1 µm target the laser intensity was comparatively lower than other two targets.

Increasing the laser intensity on target, or by lowering the target areal density beyond the values required for the formation of a sustained plasma jets, the MeV proton and ion energy spectra observed by thompson parabolas

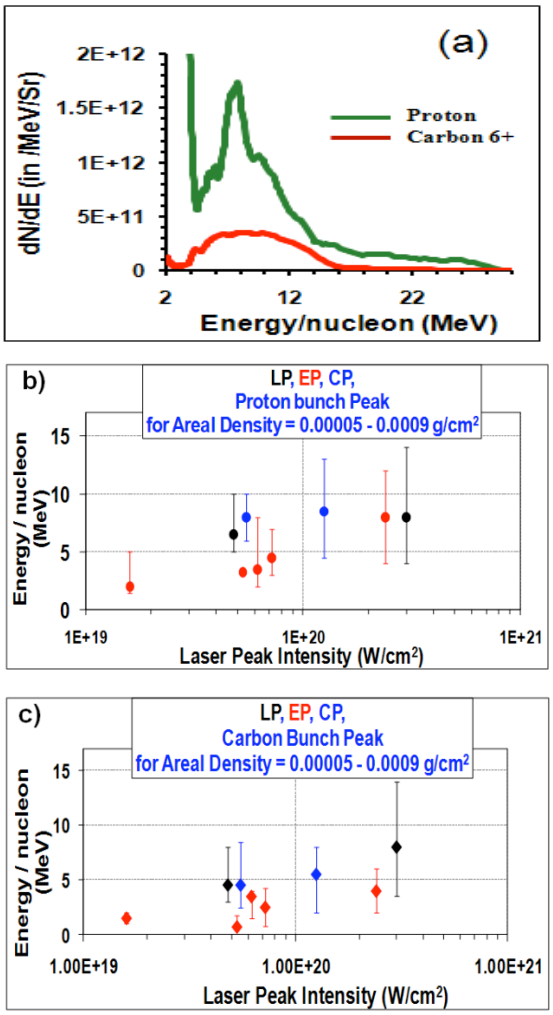

Fig. 5: (a) Ion spectra obtained from the interaction of 100 nm target at 3× 10 ^{20} W/cm^2 intensity. (b) Peak energy of proton and (c) carbon bunch at areal density of target 0.00005- 0.0009 g/cm^2 for different laser intensity. Here data points show the peak energy of bunch and error bars show the width of the bunch

become pronouncely modulated. Instread of a quasi maxwellian energy spectra for protons and carbon ions observed in the case of stable plasma jet formation regime, the spectra contains a peaked feature towards the higher energy side (fig. 5(a)). Moreover, the peaked feature in both carbon and proton spectrum lies almost close to each other over the energy/nucleon axis. Further decreasing in the target areal density or increase in laser intensity lead the bunched feature in barbon and proton spectra shifting towards higher energy (fig. 5 (b) and (c)). Priliminary 1D particle in siumulation with multiple target layers (bulk target layer with thin contaminat layers on the both sides) suggest the peaked feature in the spectra originates from the radiation pressure acceleration of contamination layer present at the laser side of the target, whereas, the exponetial low energy part in the spectrum orinates from TNSA acceleration of the target rear surface contaminant layer.

Conclusion: The dynamics and characterization of highly collimated supersonic plasma jets produced from thin targets irradiated by ultra-intense laser pulses is reported. Preliminary analysis suggests a role of the radiation pressure of the intense laser beam in the jet formation. In case of stronger drive on mass density leads the plasma jets loosing its significance and acceleration of narrow band proton and carbon spectra upto 10s of MeV per nucleon.

Acknowledgements: This work was funded by EPSRC (LIBRA Consortium, Grant No: EP/E035728/1) and by STFC Facility access. We acknowledge the support and contribution of the Target Preparation Laboratory, TAP laser staff and the Engineering workshop at CLF, RAL.

References:

[1] A.P.L. Robinson et al., New Journ. Phys. **10**, 013021(2008); A Macchi *et al*., PRL **103,** 085003 (2009)

[2] M. Koenig *et al*., Plasma and Fusion Research: Review Articles, **4**, 044 (2009)

[3] B. Loupias *et al*., PRL **99,** 265001 (2007)

[4] B. Loupias *et al*., Plasma Phys. Control. Fusion, **51,** 124027 **(**2009)

[5] C D Gregory *et al*., Plasma Phys. Control. Fusion, **50,** 124039 **(**2008)

[6] S. Kar et al., Phys Rev Lett, **100,** 225004 (2008)

[7] R. Benattar *et al.*,Rev.Sci.Instrum.**50,** 1583(1979)

[8] L. A. Gizzi *et al.*, Phys. Rev. E **49**, 5628 (1994)

Influence of overlapping high-intensity laser beams on electron and ion generation and transport

Contact *julien.fuchs@polytechnique.fr*

M. Nakatsutsumi, S. Buffechoux*, H-P. Schlenvoigt, P. Audebert, and J. Fuchs

LULI, École Polytechnique, CNRS, CEA, UPMC, route de Saclay, 91128 Palaiseau, France

*(*also with INRS-EMT, Varennes, Québec, Canada)*

G. Sarri, L. Romagnani, M. Borghesi

Centre for Plasma Physics, The Queen's University, Belfast, United Kingdom

L. Vassura

Dipartimento di Energetica, Università di Roma « La Sapienza », Roma Italy

C. L. Ellison

Princeton University, Princeton New Jersey USA

M. Cerchez, T. Toncian, and O. Willi

Institut für Laser und Plasma Physik, Heinrich-Heine Universität Düsseldorf, Universitätsstr.1, Düsseldorf, Germany

M. Quinn, O. Tresca, and P. McKenna

Department of Physics, University of Strathclyde, Glasgow, United Kingdom

R. Heathecote and R. J. Clark

Rutherford Appleton Laboratory, Didcot, United Kingdom

Introduction

Laser facilities that will explore the Fast Ignitor (FI) concept [1] are planned to comprise many bundled laser beams to produce the electron or ion beams required to achieve ignition of the pre-compressed core. For example, present planning for the HIPER FI facility [2] includes up to 42 bundled beams to reach the energy levels required for ignition. Similarly, (i) the FIREX-I laser facility in Japan, a test-bed for a planned full FI facility, will be composed of 4 bundled beams and (ii) the Omega EP facility is composed of two kJ, ps beams [3]. Up to now, most of theoretical and experimental studies of FI [4] have been performed using a single beam. For example, studies of the electron transport of GA currents using hybrid codes [5] assume that a single beam of electrons is generated. This is also the case for laser-cone FI studies, see e.g. Ref. [6]. Having multiple beams overlapping on the target could however significantly modify the end result of the interaction. Regarding electron-driven FI, the overlapping of the beams at the critical density interface could impact the generation and the potentially unstable propagation of the ultra-high current electron beams, in which the greatest uncertainties of FI still lie. Regarding ion-driven FI [7], the mixing of the hot electron sheaths emerging from the solid could be detrimental, modifying the ion acceleration process and creating spatial modulations in the global sheath that lead to unwanted caustics in the ion beam [8]. All these issues involving bundled beams need to be clarified for the FI studies to progress quantitatively. We therefore performed an experiment using two different setups addressing two topics in this context. In the first, we used two temporally separated co-linear laser beams to study the influence of having a delay between them on the plasma interaction. In the second, we used two spatially separated, quasi-orthogonal, beams to study the influence of a spatial and temporal separation between, on the plasma interaction. All these configurations were used irradiating solid (metal) targets.

Experiment

The experiment was conducted on the Vulcan TAW laser facility at the Rutherford Appleton Laboratory. This facility provided up to two independent high-energy laser pulses at the fundamental frequency (i.e. of 1053.5 nm central wavelength with a 2 nm band width). After stretching and amplification, the main Vulcan laser pulse was split into these two individual pulses (CPA#7 and CPA#8). Each laser pulse contained approximately 50 J of energy (after compression, with a pulse duration down to 1.2 ps) and was focused onto the targets using, for each, an f/3 off-axis parabolic mirror (OAP) (Fig. 1 (a)). The focal spot for each was measured to be 6.5 µm +/- 2 µm (full width half maximum) and ~35% of the energy was contained between the peak of the spot and 1/e of that peak (Fig. 1(b)). The corresponding peak intensity on target was thus ~$2x10^{19}$ W/cm^2. To detect the ions and electrons resulting for the laser interaction, we employed stacked detectors as shown in Fig. 2(a) and magnetic spectrometers, equipped with imaging plates (IPs) as detectors, placed in the forward and backward direction (with respect to the laser irradiation direction), along the target normal. For protons, we used stacked calibrated radiochromic films (RCF) (of HD-810 and MD-V2-55 type). They detected the laser-accelerated multi-MeV protons that are electrostatically accelerated by the laser-produced energetic electrons [9]. The stack was placed ~35 mm behind the target foil in the normal direction and a hole was drilled through to let the particles reach freely the rear side magnetic spectrometer.

RCFs measured the spatial distribution of proton beam at discrete energies corresponding to the proton deposited energy in the form of Bragg peaks. As also shown in Fig.2(a), for the electrons, behind the RCFs, we positioned a stack of 5 IPs separated by 1.5 mm thick Al plates (type TR2025) to resolve in

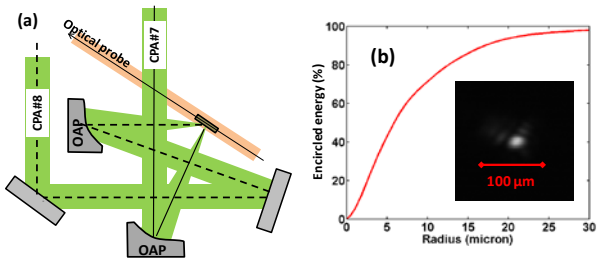

Fig. 1 (a) General layout of the experiment and CPA laser beams configuration. (b) Azimuthally averaged radial profile of a measured focal spot. (inset) Image of the focal spot.

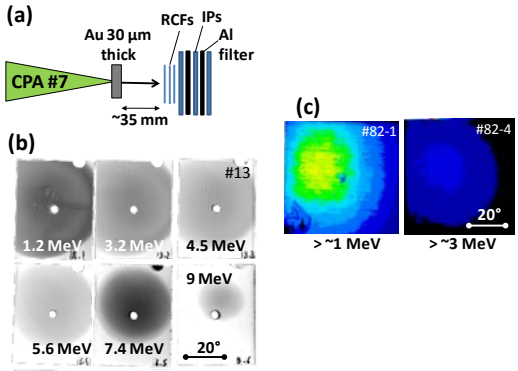

Fig. 2 (a) Setup for ions and electrons detection. (b) Typical proton beam distribution images obtained with RCFs. (c) Spatial distribution image of >1MeV and >3MeV electrons detected by the stack of imaging plates (IPs) shown in (a).

energy and angle the hot electrons [10].

In order to have a basis of comparison when we used a dual beam irradiation configuration, we first assessed the result of a single beam irradiation on target. Fig. 2(b) shows typical RCF images of the proton beam obtained in the configuration when a single laser beam interacted with a 30 µm thick Au foil. The typical maximum proton energy was 8 - 10 MeV. The divergence of the 7 MeV proton beam was around 30 degrees full angle. For the same shot, the measure of the fast electron beam divergence is shown in Fig. 2(c). The color bar here represents a logarithmic scale (QL value). In addition to these diagnostics, to assess the level of preplasma in front of the target at the time of the main laser pulse irradiation due to the laser pedestal, the plasma expansion profile of the laser-irradiated targets was diagnosed using an optical probe that was passed transversely across the target surface (as shown in Fig. 3(a) and Fig.1(a)). The probe beam was picked up from a small part of the CPA#7 that was then frequency-doubled to 2ω (527 nm). The target images were obtained with 16 bit Andor technology CCD camera (type: DX420-BN, pixel-size: 26 µm), using a 10 times magnification. To minimize the plasma self-emission signal, (I) an iris (opened ~ϕ 1mm) was placed in the imaging line at the first probe beam focal point using a f = 950 mm collecting lens. Then, (II) the signal was filtered with a ω fundamental frequency–cut filter (BG38) as well as a 2ω band pass filter (CVI Melles Griot: F10-527-4-2) that were put in front of the CCD. A typical image taken by this diagnostic for the same shot as Fig. 2(b) is shown in Fig. 3(b). The probe was timed to cross the target 10 ps after the main interaction pulse hit it. The image shows a large plasma expansion on the laser-irradiated surface of the target with extent of approximately 410 µm (transverse) and 220 µm (longitudinal). We observe that, contrary to the target front, the target rear does not exhibit any expansion, which is consistent with the high-energy proton acceleration that is observed [11]. The reference image taken just before the shot is also shown in Fig. 3(c).

The experimental setup of the first experiment investigating the energetic electron beam propagation when using two temporally separated collinear laser pulses is shown in Fig. 3(a). To achieve such irradiation configuration, the CPA#7 was spatially divided in two half-beams that could have a temporal delay between them but that were nonetheless focused on same location on the same interaction target surface (20 µm Au foils) as they both used the same focusing OAP. The relative timing of the two separated beams was adjusted by altering the path delays with ~1 ps precision using an interferometric technique. As illustrated in Fig.3(a), to diagnose

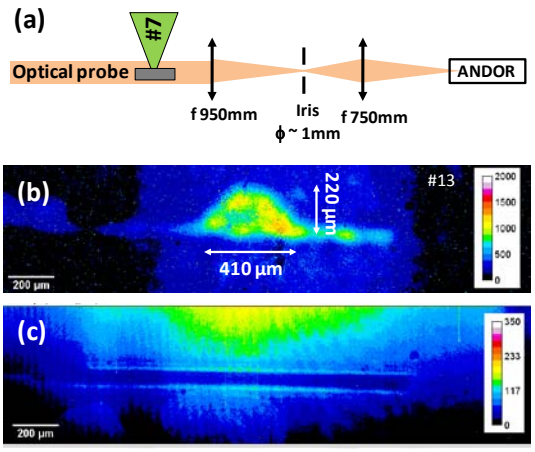

Fig. 3. (a) Setup for preplasma expansion (from the target front-surface) measurement using the optical probe beam. (b) The image corresponds to the same shot as in Fig. 2(b). It is recorded 10 ps after the interaction pulse irradiation. (c) A reference image is taken before each shot.

the result of this interaction, we used a probing proton beam that acted as a transverse charged particle probe for the fields associated with the electrons emerging from the rear of the interaction target [12]. To produce this probing beam, we used the CPA#8 that was focused onto a 25 µm thick gold foil to generate the adequate protons. The interaction targets were bent in order to minimize the deflections due to global target charge-up which would have otherwise prevented sampling of the accelerating fields. The probing proton virtual source size was small enough, so that the images can have excellent spatial resolution (~ a few µms). The multilayer arrangement of the RCF stack detector, providing a spectral resolution, allows a temporal multiframe capability. The magnification of the arrangement is given by M ~ (L + 1)/l, where l = 3 - 4 mm was the distance between the proton target and the interaction area, while L ~ 35 mm was the distance between the interaction target and the RCFs. This gives M equal to 8 – 10 in our experimental conditions. This technique is mainly sensitive to field gradients, which are detected via proton density modulations in the probe beam cross section. Figure 3(b) shows typical proton probing data obtained when the CPA#7 interaction beam was full and not split in two halves. Darker regions correspond to higher proton densities in the proton beam cross section. Each frame corresponds to a different probing time. The piling up of the probe protons with bubble-like structure appearing at later times is due to the sudden drop of the electric field ahead of the acceleration front. Such structures are similar to the ones described in [12]. When we divided temporally the CPA#7 pulse into two, the expansion velocity of the sheath was slightly decreased compare to the full beam configuration. This corresponds to the expected reduction of focal intensity of each laser by reduction of energy by half, as well as the increase of the focal spot size. The latter is because of the f-number doubling linked to the near field size reduction. However, one striking difference compared to the single laser interaction is that only in the split beam configuration did we observe, shortly after the interaction, a jet-like proton deflection pattern. Such jet had an extent of > 500 µm, and were observed reproducibly when there was a small delay (1.5 and 3 ps) between the two beams. One should note that the fast plasma expansion front from the interaction target cannot reach such a far region (> 500µm) during such a short time (< 5 ps after laser irradiation). A detailed analysis is still under way.

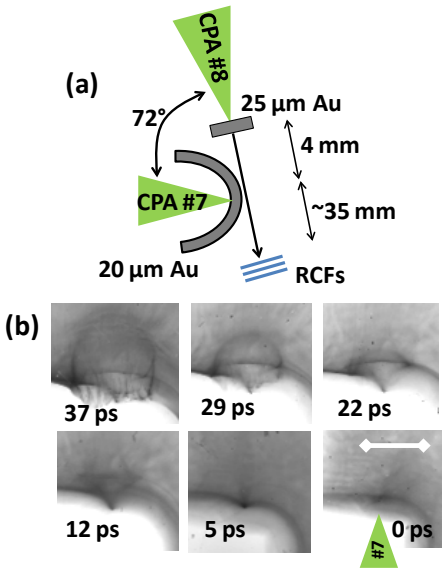

Fig. 4 (a) Experimental setup for investigating the energetic electron beam propagation when using two temporally separated collinear laser pulses. (b) Typical proton probing data obtained when the CPA#7 interaction beam was full and not split in two halves. The scale bar corresponds to 500µm in the interaction target plane. The time 0 corresponds the time when the CPA#7 arrives at the interaction target.

Figure 5 shows the other experimental setup we used to investigate the energetic electron beam propagation when using two laser pulses irradiating the targets with a large angular difference. CPA#7 and #8 then irradiated the target surface with a 72 degrees angular difference. The laser beams were synchronized such that they arrived at the surface of the gold 30 µm thick target simultaneously. In this setup, we changed the spatial separation between the laser beams over a series of shots such that the mutual separation between the laser-accelerated energetic electron beams created by each laser beam and arriving at the rear surface was comprised between -45 µm (i.e. when the lasers overlap at the target front) to ~ +150 µm. Here, as a first approximation, we assumed that the major part of electrons propagate geometrically straight along the laser axis [13]. The proton beams accelerated from the target were recorded on a stack of RCFs as well as dispersed by the magnetic spectrometer. One can expect that the sheath electrostatic fields, which have an extent of typically 100 µm [14], would overlap or partially overlap at the target rear (depending on δx) and influence the proton acceleration. Indeed, when the sheath overlapped constructively (i.e. for $|\delta x| \leq 50$ µm), we observed a clear enhancement of the accelerated proton energy by a factor of ~1.5 compared to the energy obtained in the single beam configuration. Such enhancement disappeared when we spatially separated the beams too much, as expected. Another striking feature was that we observed, in the dual beam interaction, on the RCFs a strongly collimated energetic proton beams on top of the usual diverging proton beams (see Fig. 5). As observed in all previous experiments using single-beam irradiation, the diverging proton beams showed a decrease of their divergence angle with proton energy [15], as is also seen in Fig. 1(a). Such a variation of divergence angle is expected for a transversally bell-shaped electron density distribution [14]: the highest energy protons are accelerated in the central, high-density portion of the sheath, whereas lower energies come from the wings of the sheath distribution and thus are emitted at larger angles. In contrast, a strongly collimated beam appeared in the case of dual overlapping beams. It exhibited an almost constant divergence angle (~17° full angle) when varying the proton energy. Such structure is observed repeatedly when δd is sufficiently small

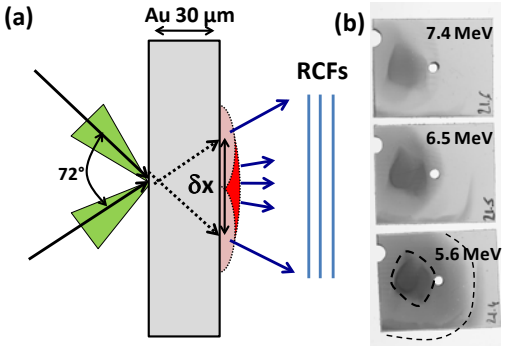

Fig. 5 (a) Experimental setup for investigating the energetic electron beam propagation when using two laser pulses irradiating the target with a large angular difference. We varied the spatial separation δx. (b) Proton distribution images obtained when the lasers overlap at the target front.

(i.e. $|\delta d| \leq 100$µm). Such collimated beam could be attributed to the overlapping of bell-shaped electrostatic sheaths. This would result in creating a plateau in the electron density profile between the two electrostatic sheathes at the target rear surface created by each laser pulse, as illustrated in Fig. 5.

Acknowledgements

We acknowledge the expert support of the Vulcan laser operation crew and engineer teams and the financial support of CLF/STFC as well as Princeton/Ecole Polytechnique and ERASMUS La Sapienza/Ecole Polytechnique exchange programs.

References

[1] M. Tabak et al., Phys. Plasmas **1**, 1626 (1994).
[2] M. Dunne, Nature Phys. **2**, 2 (2006) and HiPER—RAL Report No. RALTR-2007-008, June 2007, www.hiper-laser.org.
[3] http://www.lle.rochester.edu/05_omegalaserfacility/05_02_ep/05_ep.php
[4] S. Atzeni et al., Phys. Plasmas **15**, 056311 (2008) and references therein.
[5] J.J. Honrubia et al., Nucl. Fusion **46**, L25-L28 (2006); R. G. Evans, Plasma Phys. Controlled Fusion **49**, B87 (2007).
[6] Y. Sentoku et al., J. Phys. IV France **133**, 425–427 (2006).
[7] M. Roth et al., Phys. Rev. Lett. **86**, 436 (2001); M. Temporal et al., Phys. Plasmas **9**, 3098 (2002).
[8] J. Fuchs et al., Phys. Rev. Lett. **91**, 255002 (2003).
[9] J. Fuchs et al. Phys. Plasmas **14**, 053105 (2007).
[10] K. A. Tanaka et al. Rev. Sci. Inst. **76**, 013507 (2005). S. Buffechoux et al. Phys. Rev. Lett. (in print, 2010).
[11] J. Fuchs et al., Phys. Rev. Lett. **99**, 015002 (2007).
[12] L. Romagnani et al. Phys. Rev. Lett. **95**, 195001 (2005).
[13] R. J. Clarke et al. J. Radiol. Prot. **26**, 277 (2006).
[14] P. Antici et al. Phys. Rev. Lett. **101**, 105004 (2008).
[15] A. Mancic et al. High Energy Density Phys. **6**, 21 (2010).

Characterization of a line focus back-lighter

Contact *akr500@york.ac.uk*

A. K. Rossall, E. Wagenaars, L. M. R. Gartside, N. Booth and G. J. Tallents
Department of Physics, University of York, Heslington, York, YO10 5DD, UK

S. White and C. L. S. Lewis
Queens University Belfast, University Road, Belfast, BT71NN, Northern Ireland, UK

M. M. Notley and R. Heathcote
Central Laser Facility, STFC, Rutherford Appleton Laboratory, HSIC, Didcot, Oxon, OX11 0QX, UK

Introduction

Opacity measurements at EUV wavelengths of high energy density plasmas are difficult to undertake as the probe has to overcome the high self emission of the opaque plasma and it is difficult to create sufficiently uniform and well characterized plasma for accurate measurements. Laser produced EUV and x-ray back-lighters have been used previously to perform opacity measurements [1,2] when the flux of x-rays generated is sufficient to 'outshine' the plasma self emission. More recently, much brighter plasma based EUV lasers have been employed to probe an iron plasma [3]. In the present experiment, we set out to use a short duration (3ps) Ne-like Ge laser at 19.6nm to probe the opacity of laser heated iron.

Information regarding opacity is relevant to a number of different fields including solar and astrophysical modelling [4], inertial confinement fusion [5,6], and free-electron laser experiments [7] and there exist a number of different computer codes for simulating opacity [8,9,10,11,12]. In order to test the accuracy of these codes and solve discrepancies between them, experimental benchmark data is required.

This experiment ultimately generated an EUV back-lighter in a set-up similar to that used to create a plasma based x-ray laser, without lasing being observed. A line focus back-lighter can produce bright emission over a broad spectral range as the more intense spectral lines approach black-body intensities due to the high optical depth along the plasma line. This emission comes from a small area and can be pointed at a sample. This paper is primarily concerned with the characterisation of the back-lighter with the aim of improving our understanding of the line focus EUV back-lighter and to investigate why lasing was not observed. Accurate information regarding the plasma conditions within the EUV source is required for accurate opacity measurements. Transmission measurements through iron plasma from this experiment using EUV radiation are reported elsewhere [13].

Experiment

The back-lighter was created using two optical pulses from the VULCAN Nd:Glass laser system at the Rutherford Appleton Laboratory to irradiate a germanium target of thickness 500nm deposited onto a glass slab of 6mm width. A pre-pulse of duration 300 ps and energy of 20J was focused into a line 100µm x 6mm, using a refracting lens and a spherical mirror, giving an irradiance of ~ 8 x 10^{12} W cm^{-2}. A main (CPA) pulse of 3ps duration had an energy of 35J and was focused into a line of similar dimensions using a single f/3 off-axis parabola, giving an irradiance of ~ 1 x 10^{15} W cm^{-2}. The line foci of both beams were overlapped on the target, with a delay between the pulses of Δt=400ps.

A 50nm thick iron foil, tamped with 100nm thick parylene-N (C_8H_8) on both sides, was heated using another CPA beam from the VULCAN laser and the plasma created probed with the EUV back-lighter. The second CPA beam contained 25J energy in a duration of 1ps and was focused to a spot size of about 200µm in diameter on the opacity target. The delay between the heating pulse and the main CPA pulse was varied between 5 and 20 ps to allow probing at different stages of iron plasma evolution. Probing results have been presented elsewhere [13].

In order to characterise the line focus Ge back-lighter, a crossed-slit camera with an Andor CCD was positioned at an angle of 22 degrees with respect to the plane of the target normal. A front 15µm horizontal slit provided a vertical magnification of 3.56 with the back 100 µm vertical slit giving a horizontal magnification of 1.20. The vertical and horizontal resolution was 19µm and 180µm respectively. The crossed-slit camera was filtered using 3µm aluminium and 25µm beryllium so that emission in the range 0.5 to 5 keV was recorded. The CCD had an exposure time of 500ms so we record time integrated Ge emission over the laser plasma lifetime.

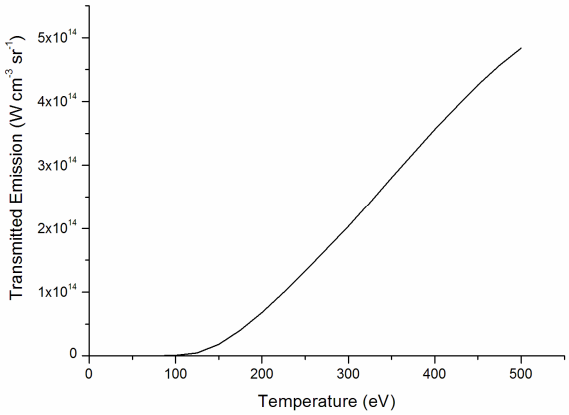

Figure 1. Spectrally integrated emission transmitted through filters of 3µm Al and 25µm Be as a function of temperature for Ge as determined with the FLYCHK code [14] and using filter transmission data from Henke et al.[15]. The electron density assumed is that seen in the region of highest gain as predicted by Ehybrid (5x10^{21} cm^{-3}).

Germanium Back-lighter Characterisation

The crossed-slit images provide an 'emission map' of the Ge back-lighter and have been characterized using simulated data from the spectral modelling code FLYCHK [14]. The code was used to evaluate total emission from the Ge plasma as a function of photon energy and temperature for the density in the region of highest gain and emission as predicted by the Ehybrid code [16] (n_e = 5 x 10^{21} cm^{-3}). Multiplying the photon energy dependant transmission [15] of the filter with the total emission and integrating over frequency gives the total emission as seen by the crossed-slit camera per unit volume (see figure 1). For our filter combination, the relationship between the transmitted emission and temperature is approximately linear in the

temperature range of 150 – 500eV, with a threshold for any significant emission at ≈ 120eV.

We assume that the plasma emission through the crossed-slit filter combination (3µm Al, 25µm Be) is dominated both spatially and temporally by the hottest temperature and highest density (5 x 10^{21} cm^{-3}) plasma. The area of plasma viewed by each pixel on the CCD is calculated using the geometry of the crossed-slit camera. A thickness of emitting plasma can be determined by calculating the plasma expansion from the turning point density by calculating the ion sound speed, v_s, for each temperature and considering a characteristic length scale, $v_s\Delta t$ (where Δt = 400ps, is the time between the pre-pulse and the main pulse). The time of emission of the plasma (100ps) is found from simulations using the 1D hydrodynamic code Ehybrid [16] (figure 2).

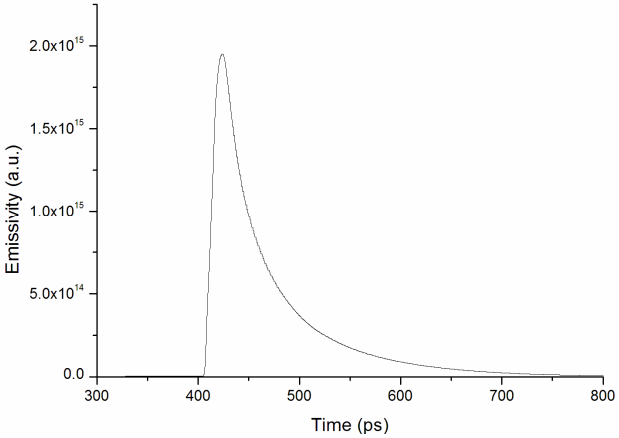

Figure 2.Emission of radiation from a Ge plasma transmitted through the filter combination for our crossed-slit camera as a function of time calculated by the Ehybrid [16] code.

A calibration factor for the CCD (8eV/count) is used to deduce the absolute number of counts per pixel associated with the transmitted emissivity. Figure 1 then enables the crossed-slit images of recorded emission to be converted to a spatial variation of electron temperature (figure 3, 4). This conversion of CCD counts to temperature is reasonably accurate (±10%) due to the rapid linear increase of emission with temperature and the threshold temperature for any significant emission (see figure 1). Our error estimate for the temperature measurement of ±10% does not include the error associated with our assumption of a spatially and temporally constant density and temperature. The incident laser intensity profile has a width of 100µm and comparing this with the deduced temperature profile width of 150µm, the relationship $T_e \propto I^{\beta}$, results in β = 0.44±0.05 in agreement with temperature scaling results [17].

Simulations using Ehybrid demonstrate peak ionisation levels in agreement with the FLYCHK model used to determine the temperature profile of the back-lighter. The peak temperature for the pre-pulse only back-lighter was found to be 120eV or less. A peak temperature of 155±20eV is found when the two pulse set-up is used. These temperatures explain the presence of spectral lines from Ge XX to GeXXIII [18,19,20,21,22] as seen in the spectrum shown in figure 5 and the significant change in emission between the pre-pulse and double pulse plasma. The figure 5 spectrum was recorded with a flat field spectrometer viewing down the line focus axis.

Although the experimental set-up was similar to that used to generate a plasma based x-ray laser, no x-ray lasing was observed and one of the motives of the present characterization of the back-lighter was to investigate why x-ray lasing was not seen. A temperature analysis of the pre-pulse only shots shows the temperature to be < 120eV, and according to ionisation curves simulated using the collisional-radiative code FLYCHK, the plasma then consists mainly of Ge^{19+} or lower ionisation stages. This ionisation is consistent with the peak ionisation determined via simulations using Ehybrid. For lasing the main pulse has to couple enough energy into the plasma to raise the ionisation level up to the Ne-like ionisation stage (Ge^{22+}) and provide the population inversion necessary for lasing, within the 3ps pulse length.

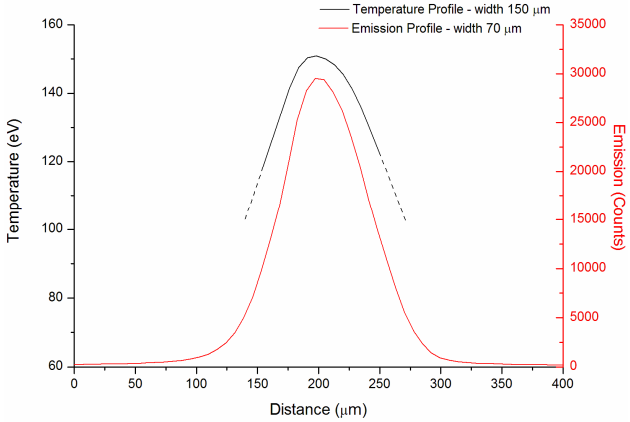

Figure 3. Emission cross-section over the line profile and the resulting temperature profile deduced as discussed in the text.

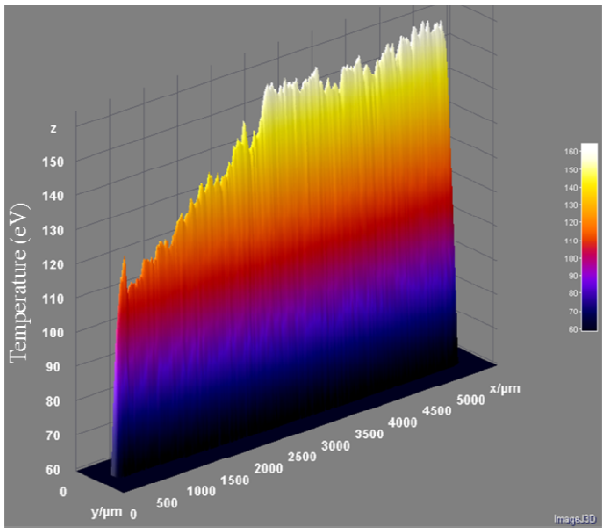

Figure 4. 2D temperature profile of the Ge back-lighter.

Due to the short pulse duration (3ps) of the laser, the main pulse energy is largely coupled at higher densities, meaning any x-ray laser photons produced may be refracted out of the gain medium, reducing amplification. This effect has been reported previously by Smith et al. [23] and so has been investigated through simulations with Ehybrid (see figure 6).

Ehybrid demonstrates that the experiment produces the maximum gain within the Ge plasma at a density of 5 x 10^{21} cm^{-3}. The region of gain as simulated by Ehybrid has width Δs ≈ 4µm (figure 6) and has a peak gain value of G=200 cm^{-1}. Refraction at such high densities is significant. We can write that the refraction angle θ is related to the density scale length Δx and electron density n_e by [24]

$$\theta \approx \frac{L}{\Delta x}\frac{n_e}{2n_c}$$

where n_c is the x-ray laser critical density. Setting the maximum refraction angle $\theta = \Delta s/L$, gives that the x-ray laser propagation distance L in the gain region is such that

$$L \leq \sqrt{\Delta s \Delta x \frac{2n_c}{n_e}}.$$

For Δs = 4μm, n_e = 5 x 10^{21} cm^{-3} and density gradient as shown in figure 6, we obtain $L \leq 100$ μm, implying maximum gain length product $GL \leq 2$ which would not be observable.

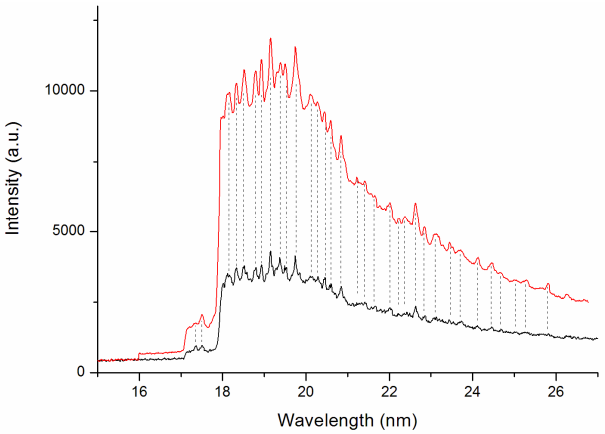

Figure 5. Ge spectrum as recorded by a flat field spectrometer. The red line demonstrates the spectrum originating from a back-lighter created using the two-pulse setup and the black line shows the spectrum from a back-lighter created using only the pre-pulse. The drop in intensity at 18nm is due to the CCD chip being partially covered with aluminium. The intensity drop at 17nm is the aluminium K edge.

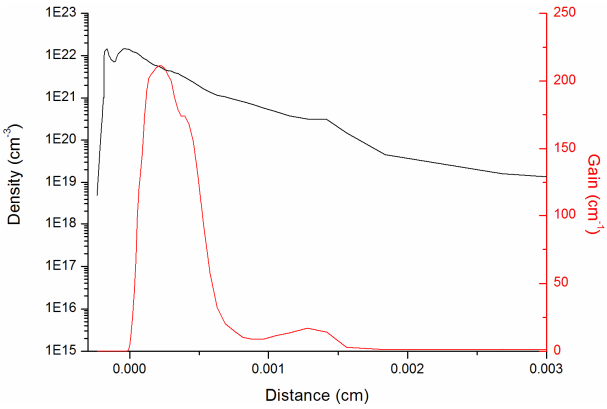

Figure 6. Density and small signal gain profile at the time of peak gain, t=409ps, 6ps after the end of the main CPA pulse as simulated by Ehybrid for the conditions of the experiment.

Conclusions

This experiment has demonstrated how a plasma back-lighter can be well characterized through imaging the time and spectrally integrated emission profile of the plasma using a crossed-slit camera. By applying a detailed model of emission to the back-lighter images, a spatially dependant electron temperature profile can be inferred and used as a useful diagnostic of the plasma. Further study has shown the pulse duration of the main CPA pulse not to be ideal for lasing. Simulations using Ehybrid demonstrate that the short pulse duration and other conditions of the experiment result in energy coupling at higher densities where the increased refraction deflects lasing photons out of the gain region inhibiting amplification.

Acknowledgements

We acknowledge funding from the UK Engineering and Physical Sciences Research Council (EPSRC) and the Science and Technology Facilities Council (STFC) for this work. We would also like to thank the staff at the Central Laser Facility, Rutherford Appleton Laboratory for their assistance.

References

[1] S. Davidson, J. Foster, C. Smith, K. Warburton, and S. J. Rose, Applied Physics Letters **52**, 847 (1988).

[2] T. Perry, S. Davidson, F. Serduke, D. Bach, C. Smith, J. Foster, R. Doyas, R. Ward, C. Iglesias, F. Rogers, J. Abdallah, R. Stewart, J. Kilkenny, and R. Lee, Physical Review Letters **67**, 3784-3787 (1991).

[3] M. Edwards, D. Whittaker, P. Mistry, N. Booth, G. Pert, G. Tallents, B. Rus, T. Mocek, M. Koslová, C. McKenna, A. Delserieys, C. Lewis, M. Notley, and D. Neely, Physical Review Letters **97**, (2006).

[4] G. B. Rybicki and A. P. Lightman, *Radiative Processes In Astrophysics* (Wiley VCH, 1985), p. 400.

[5] E. Mínguez, P. Martel, J. M. Gil, J. G. Rubiano, and R. Rodríguez, Fusion Engineering And Design **60**, 8 (2002).

[6] J. E. Bailey, G. A. Chandler, R. C. Mancini, S. A. Slutz, G. A. Rochau, M. Bump, T. J. Buris-Mog, G. Cooper, G. Dunham, I. Golovkin, J. D. Kilkenny, P. W. Lake, R. J. Leeper, R. Lemke, J. J. MacFarlane, T. A. Mehlhorn, T. C. Moore, T. J. Nash, A. Nikroo, D. S. Nielsen, K. L. Peterson, C. L. Ruiz, D. G. Schroen, D. Steinman, and W. Varnum, Physics Of Plasmas **13**, 056301 (2006).

[7] S. M. Vinko, G. Gregori, M. P. Desjarlais, B. Nagler, T. J. Whitcher, R. W. Lee, P. Audebert, and J. S. Wark, High Energy Density Physics **5**, 124-131 (2009).

[8] S J Rose, Journal Of Physics B: Atomic, Molecular And Optical Physics **25**, 1667 (1992).

[9] N. H. Magee, Jr. Abdallah, J., R. E. H. Clark, J. S. Cohen, L. A. Collins, G. Csanak, C. J. Fontes, A. Gauger, J. J. Keady, D. P. Kilcrease, and A. L. Merts, Astron. Soc. Of The Pacific Conf. Ser. **78**, 51 (1995).

[10] F. J. Iglesias, C. A. And Rogers, Astrophys. J. **464**, 943 (1996).

[11] M. J. Seaton, Y. Yan, D. Mihalas, and A. K. Pradhan, R.A.S. MONTHLY NOTICES V.266 805-828 (1994).

[12] B. Crowley, Journal Of Quantitative Spectroscopy And Radiative Transfer **71**, 257-272 (2001).

[13] E. Wagenaars, L. M. R. Gartside, A. K. Rossall, N. Booth, S. White, C. L. S. Lewis, M. M. Notley, R. Heathcote, and G. J. Tallents, in *Soft X-Ray Lasers And Applications VIII*, James Dunn and Gregory J. Tallents (SPIE, San Diego, CA, USA, 2009), pp. 74510G-8.

[14] H. Chung, M. Chen, W. Morgan, Y. Ralchenko, and R. Lee, High Energy Density Physics **1**, 3-12 (2005).

[15] B. Henke, Atomic Data And Nuclear Data Tables **54**, 181-342 (1993).

[16] G. J. Pert, Journal Of Fluid Mechanics **131**, 401 (1983).

[17] H. Puell, H. J. Neusser, and W. Kaiser, Z. Naturforsch A **25**, 1815 (1970).

[18] G P Gupta and A Z Msezane, Physica Scripta **77**, 035303 (2008).

[19] Joseph Reader, Victor Kaufman, Jack Sugar, Jan Olof Ekberg, U. Feldman, C. M. Brown, J. F. Seely, and W. L. Rowan, Journal Of The Optical Society Of America B **4**, 1821 (1987).

[20] J O Ekberg, A Redfors, C M Brown, U Feldman, and J F Seely, Physica Scripta **44**, 539-547 (1991).

[21] G Yuan, Y Kato, H Daido, R Kodama, K Murai, and T Kagawa, Physica Scripta **53**, 197-203 (1996).

[22] B. C. Fawcett and R. W. Hayes, Journal Of The Optical Society Of America **65**, 623 (1975).

[23] R. Smith, J. Dunn, J. Filevich, S. Moon, J. Nilsen, R. Keenan, V. Shlyaptsev, J. Rocca, J. Hunter, and M. Marconi, Physical Review E **72**, 036404 (2005).

[24] G J Tallents, Journal Of Physics D: Applied Physics **36**, R259-R276 (2003).

Creation of persistent, straight, 2mm long laser-driven channels in underdense plasmas for Fast Ignition applications

G. Sarri[1], J. R. Davies[2], K.L. Lancaster[3], E.L. Clark[4], S. Hassan[4], J. Jiang[2], N. Kageiwa[5], N. Lopes[2], A. Rehman[6], C. Russo[2], R.H.H. Scott[3,6], T. Tanimoto[5], Z. Najmudin[6], K.A. Tanaka[5], M. Tatarakis[4], M. Borghesi[1] and P.A. Norreys[3,6]

[1] *School of Mathematics and Physics, Queens University Belfast, BT7 1NN, UK*

[2] *GoLP, Instituto de Plasmas e Fusão Nuclear - Laboratório Associado, Instituto Superior Técnico, 1049-001 Lisbon, Portugal*

[3] *STFC Rutherford Appleton Laboratory, Didcot, OX11 0QX, UK*

[4] *Technological Educational Institute of Crete, GR 710 04 Greece*

[5] *Graduate School of Engineering, Osaka 565-0871, Japan*

[6] *Blackett Laboratory, Imperial College London, London SW7 2BZ UK*

Abstract

The experimental study of the behavior of deuterium plasma with densities between 2×10^{18} and $2\times10^{20}\mathrm{cm}^{-3}$, subjected to a 6 TW, 30 ps, $3\times10^{18}\mathrm{Wcm}^{-2}$ laser pulse, is presented. Conclusive experimental proof is provided that a single straight channel is generated when the laser pulse interacts only with the lowest densities. This channel shows no small-scale longitudinal density modulations, extends up to 2 mm in length and persists for up to 150 ps after the peak of the interaction. Bifurcation of the channel after 1 mm propagation distance is observed for the first time. For higher density interactions, above the relativistic self-focusing threshold, bubble-like structures are observed to form at late times. These observations have implications for both laser wakefield accelerators and fast ignition inertial fusion studies.

Introduction

There are a number of applications of intense laser pulses that require the formation of a stable channel in an underdense plasma [1, 2]. These include quality control of multi-MeV electron bunches generated in laser wakefield accelerators [3–5], particularly the reproducibility and selection of the bunch energy [6], as well as high brightness X-ray generation in these channels by betratron oscillations [7] and fast ignition inertial confinement fusion (FI) [8]. In the latter case, Tabak et al. [8] proposed to add a hundred of picoseconds scale pedestal to the ignition pulse, in order to generate a channel through the underdense plasma and to push the critical surface close to the pre-compressed fuel. Such a channel would then allow the ignition pulse to propagate practically undisturbed through the mm-scale coronal plasma surrounding the dense fuel. This scheme has several advantages compared to the alternative cone-guided concept which has already demonstrated, in small-scale experiments, efficient coupling between petawatt pulses and the core [9]. Firstly, it promises less complex target manufacture, allowing low-cost mass production for inertial fusion energy purposes. Secondly, it allows targets with a higher degree of spherical symmetry to be compressed.

In the past few years, channeling driven by high intensity laser pulses has been extensively studied in a number of experiments (e.g. [10–13]) mainly by optical interferometric techniques, as well as X-UV radiography [14]. These experiments concerned either short duration laser pulses ($\leq$ 1 ps) or relatively small observation distances ($\leq$ 0.2 mm). All these interactions, however, employed relativistic laser pulses; in this regime, detrimental instabilities such as longitudinal modulations induced by relativistic self-focusing [13], long wavelength hosing [13] and self modulation [10] have been seen to occur.

Li et al. [15] have shown, with the aid of 2D Particle-In-Cell (PIC) simulations, that stable channels can be generated when a pulse of sufficiently long duration is used; the sustained ponderomotive pressure eventually wins over the instabilities. These simulations were run with regard to a plasma density in the range $0.1n_c \geq n_e \geq 1.02n_c$. However, a directly driven, ignition scale implosion will generate a large region of less dense plasma ahead of the compressed fuel.

Therefore, as part of the HiPER project [16], an experiment was conducted on the Vulcan laser facility at the Rutherford Appleton Laboratory [17] whose specific aim was to study laser channeling in underdense plasma. The experiment used a laser pulse, emulating the one proposed by Li et al. [15], focused onto a supersonic deuterium gasjet with variable density. Here, the results of this experiment are presented. It is demonstrated that, when the power of the laser pulse is below the threshold for relativistic self-focusing, the sole

ponderomotive force is able to create a longitudinally smooth channel extending for the whole gasjet extension (i.e. 2 mm) and persisiting for up to 150ps. The channel formation has been reproduced in matching 2D PIC simulations of this experiment.

Experimental setup and raw data

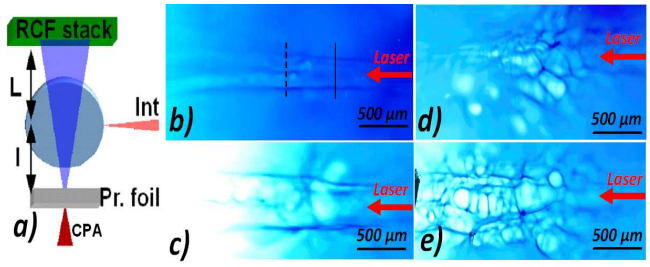

Figure 1: **a.** Schematic top-view of the experimental setup. **b.** $n_e = 2 \times 10^{-3} n_c$, $t_{prob} = 100$ps. **c.** $n_e = 2 \times 10^{-3} n_c$, $t_{prob} = 150$ps. **d.** $n_e = 2 \times 10^{-1} n_c$, $t_{prob} = 100$ps. **b.** $n_e = 2 \times 10^{-2} n_c$, $t_{prob} = 100$ps. All the radiographs refer to a probing proton energy of 4 MeV

.

The gasjet backing pressures chosen were to be in the range 1 - 100 bars corresponding, once fully ionised, to $n_e = 2 \times 10^{18}\text{cm}^{-3}$ - $2 \times 10^{20}\text{cm}^{-3}$ (i.e. $2 \times 10^{-3} - 2 \times 10^{-1} n_c$). The laser parameter were as follows: $\tau_L = 30$ps, $P_L = 6$ TW, $I\lambda^2 = 3 \times 10^{18}\text{Wcm}^{-2}\mu\text{m}^{-2}$. The laser power was sufficient to study conditions below and above the threshold for relativistic self-focusing, given by $P_{cr} = 17(n_c/n_e)$GW [18]. The interaction was probed in the transverse direction via the proton radiography technique [19] by the use of a high fidelity proton beam created during the interaction of a second laser beam (pulse duration 1 ps, energy $E = 60$ J and intensity 10^{19} Wcm^{-2}) with a 20 μm thick metallic foil (see Fig.1.a for a sketch of the setup). The proton beam, after having probed the plasma, was recorded on a stack of dosimetrically calibrated RadioChromic Films (RCF), [20] geometrically magnified by a factor of $M \approx L/l \approx 6$ (Fig. 1.a). The proton probe was timed to traverse the plasma at $t_{prob} = 100 - 150$ ps after the peak of the 30-ps duration interaction pulse.

Typical data showing the features observed by proton imaging for $n_e = 2 \times 10^{-3} n_c$ are displayed in Figs. 1.b and 1.c Fig. 1.b shows that, at 100 ps after the peak of the interaction, a channel, 300 μm wide, is present with sharp edges for the entire length of the gas jet itself and no longitudinal modulations can be seen within the channel, in contrast to previous experimental observations [10, 11, 13]. The channels starts to deteriorate only after 150 ps (Fig. 1.c).

For densities laying above the threshold for relativistic self-focussing, persistent bubble-like structures were observed both outside and within the channel (see Fig. 1.d and 1.e). In this regime, the channel does not survive unperturbed during the time when the proton beam traversed the plasma at late times.

An interesting feature arising directly from the observation of the raw data for the smooth channel is its apparent bifurcation in the center of the gas jet in Fig. 1.b.

Discussion

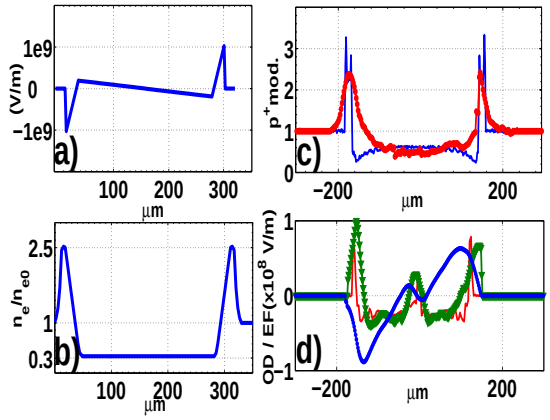

Figure 2: **a.** 1D profile of the electric field distribution used as the input for the PT simulations. **b.** Related electron density normalized to $2 \times 10^{18}\text{cm}^{-3}$. **c.** Red line: experimental proton modulation across the channel (solid line in Fig.1.b). Blue line: PT simulated proton density modulation. **d.** Green triangles: experimental optical density modulation across the bifurcated region (dashed line in Fig.1.b). Red line: optical density from the related PT simulation. Blue line: experimental electric field distribution.

In order to estimate the electron density modulation across the channel associated with the proton modulation recorded by the RCFs, Particle Tracing (PT) simulations of the propagation of the probing proton beam through the plasma have been performed for both the bifurcated and single channel regions. This code tracks proton trajectories of specified energies (4 MeV in the present work) from a point-like source through a time-dependent 3D electric field distribution up to the proton detector. This provides a 2D proton density mapping at the detector plane. For the case of the single channel region, the simulation is only able to reproduce the relevant features of its radiographic image provided that an electric field, symmetric along the laser propagation axis, (shown in Fig 2.a with the related electron density distribution shown in Fig 2.b) is assumed. This is consistent with a piling up of the plasma density up to 2-3 times the background density

at the channel walls and an inner density depletion of $\approx 70\%$. A comparison between the measured proton probe beam modulation at the RCF plane (along the lineout highlighted in Fig. 1.b) and the simulation is shown in Fig. 2.c, revealing close agreement. For the bifurcated channel, the code reproduces the features visible in Fig. 1.b only if two different cylindrically symmetric sub-channels, similar in shape to the single channel, are assumed (see Fig 2.d for a comparison between the experimental and simulated optical density results). This confirms that the channel does split into two cylindrically symmetric sub-channels.

Two-dimensional particle-in-cell (PIC) simulations have been carried out using the code OSIRIS [21]. A fully ionised deuteron-electron plasma has been assumed; its density profile is exponential with 50 μm scalelength until it reaches 1% of the critical density, and constant after that. Laser parameters are as follows: amplitude $a_0 = 1.0$, corresponding to 10^{18} Wcm^{-2}, 10 μm spot diameter, 20 ps FWHM duration; the laser is polarised along the x_2 axis.

Simulation reveals that a plasma channel is formed with steep walls (2-2.5 times the background density n_b) and a low density near its axis (0.1-0.2 times n_b). This is similar to the experimental results, apart from the widening of the experimental channel and the dulling of its walls, brought about by its evolution in time (100 ps versus 16 ps). It has to be noted that a slightly higher initial density is needed as a simulation parameter in order to match the experimental data basically due to geometrical reasons: a 2D geometry in fact confines less the laser. We repeated in fact the simulation at a lower density of $0.002 n_c$, matching the density used in the experiments more closely. The channel formation process was basically identical, but the self-focusing was less prominent, leading to a creation of 4 rather than 2 parallel beamlets.

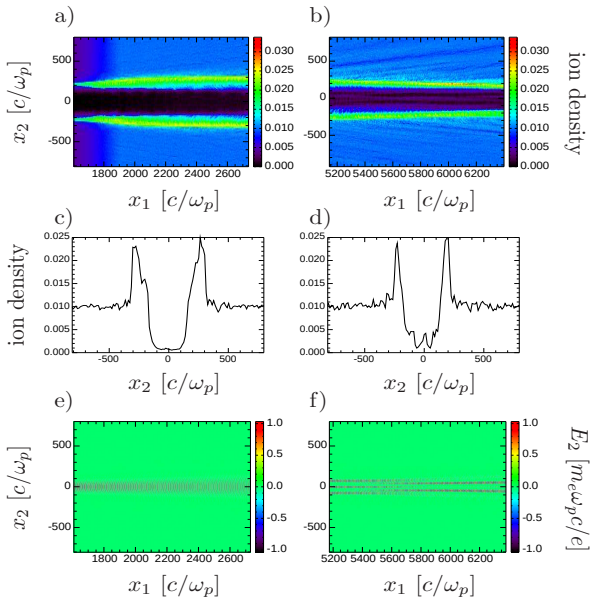

Figure 3: Simulated ion density and laser electric field distribution for both the single (images **a.** and **e.**) and bifurcated regions (images **b.** and **f.**). Images **c.** and **d.** show transverse crosscuts of images **a.** and **b.** respectively.

Conclusions

In conclusion, the experimental study of channeling driven by a 6 TW, 30 ps laser pulse through an underdense deuterium plasma has been presented. Below the regime of relativistic self-focussing, the sole classical ponderomotive force is able to drill a stable and smooth channel, ideal for subsequent pulse guiding through the large regions of tenuous plasma in a direct drive fast ignition scenario. Multi-dimensional PIC and particle tracing simulations of the laser-driven channel formation show good agreement with the experimental observations.

[1] C.G. Durfee III and H. M. Milchberg, Phys. Rev. Lett. **71**, 2409 (1993).
[2] K. Krushelnick *et al.*, Phys. Rev. Lett. **78**, 4047 (1997).
[3] W.P. Leemans *et al.* Nature Phys. **2**, 696 (2006).
[4] T. Rowlands-Rees *et al.* Phys. Rev. Lett. **100**, 105005 (2008).
[5] A.G.R. Thomas *et al.* Phys. Rev. Lett. **100**, 255002 (2008).
[6] J. Faure *et al.* Nature (London) **444**, 737 (2006).
[7] S. Kneip *et al.* Phys. Rev. Lett. **100** 105006 (2008).
[8] M. Tabak *et al.* Phys. Plasmas **1**, 1626 (1994).
[9] R. Kodama *et al.* Nature (London) **412**, 798 (2001).
[10] M. Borghesi *et al.* Phys. Rev. Lett. **78**, 879 (1997).
[11] J. Fuchs *et al.* Phys. Rev. Lett. **80**, 8 (1998).
[12] K. A. Tanaka *et al.* Phys. Rev. E **60**, 3283 (1999).
[13] Z. Najmudin *et al.* Phys. Plasmas **10**, 438 (2003).
[14] K. Takahashi *et al.* Phys. Rev. Lett. **84**, 2405 (2000).
[15] G. Li *et al.* Phys. Rev. Lett. **100**, 125002 (2008).
[16] M. Dunne Nature Phys. **2**, 2 (2006).
[17] C. Hernandez-Gomez *et al.* RAL report no. RAL-TR-2008-025, p. 260, ISBN 978-0-9556616-4-8 (2008).
[18] P. Sprangle, C.-M. Tang, and E. Esarey, IEEE Trans. Plas. Sci. **15**, 145 (1987).
[19] G. Sarri *et al.* New Jour. Phys. **12**,045006 (2010).
[20] J. F. Dempsey *et al.* Med. Phys. **27**,10 (2000).
[21] R.A. Fonseca, L.O. Silva, R.G. Hemker, *et al.* Lect. Not. Comp. Sci. **2331**, 342 (2002).

Observation of post-soliton expansion following laser propagation through an underdense plasma

G. Sarri[1], D. K. Singh[2], J. R. Davies[2], K.L. Lancaster[3], E.L. Clark[4], S. Hassan[4], J. Jiang[2], N. Kageiwa[5], N. Lopes[2], A. Rehman[6], C. Russo[2], R.H.H. Scott[3,6], T. Tanimoto[5], Z. Najmudin[6], K.A. Tanaka[5], M. Tatarakis[4], M. Borghesi[1] and P.A. Norreys[3,6]

[1] *School of Mathematics and Physics, Queens University Belfast, BT7 1NN, UK*

[2] *GoLP, Instituto de Plasmas e Fusão Nuclear - Laboratório Associado, Instituto Superior Técnico, 1049-001 Lisbon, Portugal*

[3] *STFC Rutherford Appleton Laboratory, Didcot, OX11 0QX, UK*

[4] *Technological Educational Institute of Crete, GR 710 04 Greece*

[5] *Graduate School of Engineering, Osaka 565-0871, Japan*

[6] *Blackett Laboratory, Imperial College London, London SW7 2BZ UK*

(Dated: 29th June 2010)

Abstract

The expansion of electromagnetic post-solitons emerging from the interaction of an intense laser pulse with an underdense plasma has been observed up to 100 ps after the pulse propagation, when large numbers of post-solitons were seen to remain in the plasma. The temporal evolution of the post-solitons has been accurately characterized with a high spatial and temporal resolution. The observed expansion is compared to analytical models and three dimensional particle-in-cell results providing indication of the polarisation dependence of the post-soliton dynamics.

The experimental characterization of such structures is of fundamental importance for high intensity laser-plasma physics studies since they are the major responsible for the dissipation of the laser energy.

Introduction

During its propagation through an underdense plasma, the laser experiences a significant energy loss. Being this energy loss fully adiabatic, it is mostly translated into a red shift of the laser light [6]. In the case of initial plasma densities close to the critical density, this frequency decrease may eventually lead the laser to locally experience an overcritical plasma, thus being trapped in plasma cavities. These cavities, whose radius is of the order of the electron collisionless skin depth ($l_e = c/\omega_{pe}$, where ω_{pe} is the Langmuir plasma frequency) are usually referred as electromagnetic (e.m.) sub-cycle solitons [4]. These structures tend to be accelerated along plasma density gradients [3, 7] and, therefore, are slowly propagating, if not steady, in a homogeneous plasma. For times longer than the ion plasma period, the Coulomb repulsion of the ions left inside the cavity causes it to radially expand, and the soliton nature is lost: such late-time evolution of a soliton is thus commonly referred as a *post-soliton* [8]. This mechanism is similar to the Coulomb explosion that occurs inside laser channels following relativistic self-focussing [1].

Post-soliton expansion has been analytically studied [8, 9], using the so-called snowplow model [10] and the isolated spherical resonator model [11], and numerically, using Particle-In-Cell (PIC) codes [8]. Experimental observation of post-soliton structures was first reported in [12], where soliton remnants were observed in the dense region of a plasma resulting from the laser-driven explosion of a thin foil. Due to the nature of the plasma employed, clouds of bubble-like structures were detected thus preventing a precise characterisation of the temporal evolution of the post-solitons.

Here, we report the first experimental observation of well isolated post-soliton structures. This allows their evolution to be resolved and followed over a significant temporal window. The experimental results are compared to analytical and three dimensional (3D) PIC code models.

Experimental setup and raw data

The experiment was carried out at the Rutherford Appleton Laboratory employing the VULCAN Nd:glass laser operating in the chirped pulse amplification mode [13]. A sketch of the set up is given in Fig. 1: 200 J of 1 μm laser light contained in a 30 ps Full Width Half Maximum pulse ("Int" in Fig. 1) were focussed to a peak intensity of 3×10^{18} W cm^{-2} at the edge of a supersonic deuterium gas jet with a backing pressure ranging from 1 to 100 bar. This resulted, once fully ionized, in an electron density of 10^{18}–10^{20} cm^{-3}, which is 0.001–0.1 times the non-relativistic critical density n_c. The interaction was diagnosed via the proton radiography technique [12, 14], which uses, as a particle probe, a laser accelerated proton beam, arising

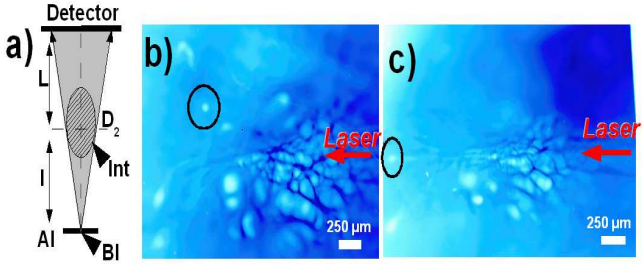

Figure 1: **a)** Top view of the experimental arrangement. **b), c)** Radiographs of two different shots: outlined with dark circles are the density bubbles interpreted to be post-solitons.

from the interaction of a secondary laser pulse ($\tau \approx 1$ ps, $E \approx 100$ J, $I \geq 10^{19}$ W cm^{-2}, "Bl" in Fig. 1) with a 20μm thick aluminium foil. The virtual point-like source [15] allows imaging of the interaction area with a geometrical magnification $M \approx (l + L)/l \approx 6$, where $l \approx 6$ mm and $L \approx 3$ cm, see Fig. 1.a. The probe beam, after having passed through the gas jet, was recorded by a stack of RadioChromic Films (RCF) [16].

The data set comprised about 30 shots in which both the deuterium density and the probe time were varied. Two typical proton radiographs obtained at a density of $0.1n_c$ are shown in Fig. 1. These images were obtained with protons of energy ≈ 4 MeV, 100 ps after the beginning of the interaction. As a rule of thumb, the electric fields are directed from the regions of lighter blue color (reduced proton flux) towards the regions of darker blue color (increased flux). In both images, a channel created by the laser pulse is visible in the low density region at the edge of the gas jet. In the dense region inside the gas jet a strongly modulated deflection pattern is visible along the laser propagation axis. This scaly region highlights the presence of a cloud of bubbles that appear merged or overlying one another in this 2D projection, possibly surrounding the laser-driven channel. Such a region visually resembles the cloud of solitons that was experimentally and numerically observed in [12]. Ahead of and around this region, isolated bubble-like structures are visible (black circles in Fig. 1), most of them located at the end of laser filaments, as numerically predicted in [3]. These bubbles are associated with strong probe proton depletion with sharp edges. We note that bubble-like structures were never seen at electron densities of $0.01n_c$ or less. We ascribe these bubbles to post-solitons.

Discussion

Considering the isolated bubbles allows following the fundamental properties of the post-solitons temporal evolution. Thanks to the multi-frame capability of proton radiography [14], it is possible to follow their temporal evolution of these bubbles in the range 80–130

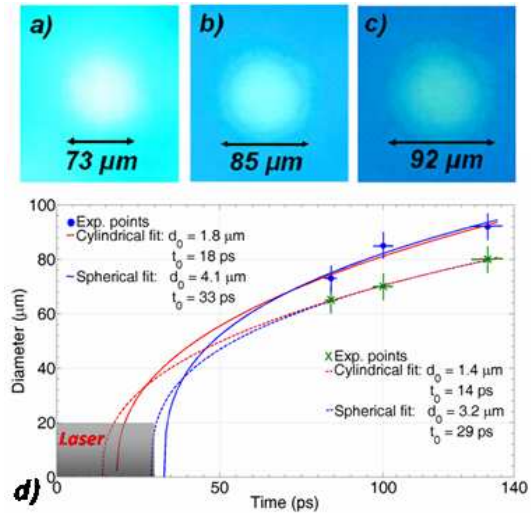

Figure 2: Zoom in on the bubble structure outlined in Fig. 1 in different layers of the RCF stack corresponding to 84 ps (**a)**), 100 ps (**b)**) and 132 ps (**c)**). **d)** Bubble diameter as a function of time and fits using results from the snowplow model for cylindrical and spherical post-solitons.

ps after the beginning of the interaction, i.e. 40–90 ps after the laser has left the gas jet. Both bubbles analyzed were found to be effectively stationary in the laboratory reference frame and to expand preserving a roughly circular shape (Fig. 2).

Bulanov and Pegoraro [9] give analytical results for the expansion of 1D planar, 2D cylindrical and 3D spherical post-solitons using the snowplow model. In 3D the diameter of the sphere is given by $d_0(3^{3/2}t/t_s)^{1/3}$ for $t \gg t_s$, where t_s is given by $\sqrt{2\pi d_0^2 n_0 m_i / \langle E_0^2 \rangle}$, d_0 is the initial diameter, n_0 is the initial ion density, m_i is the ion mass and $\langle E_0^2 \rangle$ is the time average of the square of the initial oscillating electric field inside the post-soliton. We fitted the experimental results with this function taking the initial diameter d_0 and the time of creation of the soliton t_0 as free parameters and $\langle E_0^2 \rangle^{1/2} = 2 \times 10^{12}$ V m^{-1}, which is roughly the average value of 40% of the initial laser field. Even though this function was able to fit the experimental data (see Fig. 2), it implied a creation time at the end of, if not after, the laser pulse duration, which is not physically sensible. We therefore tried the 2D cylindrical result $d_0(5t/t_s)^{2/5}$: this gave a more physically meaningful fit with a creation time close to the peak of the laser pulse in both cases. The initial diameters from the cylindrical fits are also more reasonable than those from the spherical fits, being ≈ 1 μm instead of ≈ 3 μm, since we have $c/\omega_{pe} \approx 0.53$ μm (see Fig. 2 for the fits result). Other bubbles in Fig. 1 and in different shots (not shown) have been found to expand in a similar fashion.

In order to understand why a 3D structure follows predictions for 2 rather than 3 dimensions, we carried out a 3D run with the PIC code OSIRIS [17]. We considered a linearly polarized laser pulse with a wavelength of 1 μm, Gaussian spatial and temporal profiles with FWHM of 6 μm and 1 ps, respectively, and a peak intensity of 3×10^{18} W cm^{-2} incident on a fully ionized deuterium plasma with a density of $0.1 n_c$. The interaction was followed for 5 ps. The simulation box was $350 \times 50 \times 50$ μm, divided into 2.4×10^8 cells each having 2 particles for electrons and 2 for deuterium ions, the time step was 0.196 fs. A number of longer 2D runs, with a larger number of particles per cell and a range of plasma densities, were also carried out for s-polarization (laser electric field out of the plane) and p-polarization (laser electric field in the plane). The ion density in Fig. 3.b shows prolate spheroid post-solitons, with an aspect ratio of 5:3, lying outside the channel formed by the laser in the plane perpendicular to the laser electric field. In the 2D runs solitons were only ever formed for s-polarized light (see, for instance Fig. 3.a). This dependence of soliton creation upon the laser polarization is in line with the PIC code results reported in [3]. The solitons were formed as the result of laser leakage due to its breaking-up in filaments that led to the creation of sub-channels departing from the main channel (as visible in both Figs 3.a and 3.b).

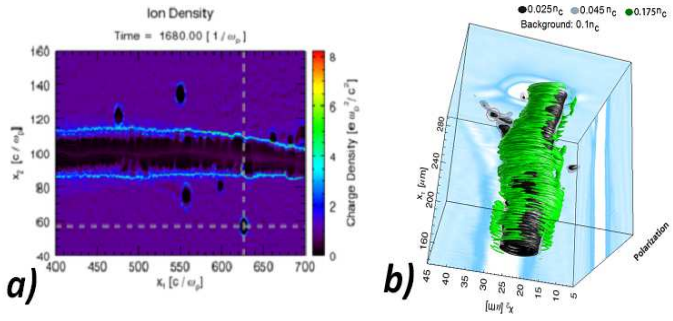

Figure 3: **a)** Ion density at 3ps from 2D PIC modeling for s-polarized light. **b)** Iso-surfaces of the ion density at 4.11 ps from 3D PIC modeling. Sub-channels are formed in the s-plane (perpendicular to the laser electric field) following leakage of the laser from the channel formed. Several post-solitons are located in these sub-channels.

The non-spherical shape of the post-solitons gives a first indication as to why the spherical scaling may not apply. The observed polarization dependence of soliton formation suggests why the spherical scaling does not apply. The snowplow model assumes in fact total reflection of the trapped light at the overcritical soliton wall and therefore no plasma heating. This is a good approximation only for s-polarized light, since a p-polarized wave will be indeed absorbed by the overcritical walls [18]. This might explain why p-polarized light is not able to excite stable e.m. solitons [3].

Conclusions

In conclusion, we have reported the first experimental measurements of the late time expansion of post-solitons following the propagation of a relativistically intense laser pulse through an underdense plasma. The post-soliton expansion has been temporally resolved with high temporal and spatial resolution. The post-soliton expansion is best described by the analytical prediction for cylindrical, not spherical, post-solitons. 3D and 2D PIC code results suggest that this is due to polarization effects.

[1] A. G. Litvak, Sov. Phys. JETP **30**,344 (1969); P. Sprangle *et al.*, IEEE Trans. Plasma Sci., **PS-15**,145 (1987)
[2] D. Farina and S. V. Bulanov, Phys. Rev. Lett., **86**,5289 (2001).
[3] S. V. Bulanov *et al.*, Phys. Rev. Lett., **82**,3440 (1999).
[4] T. Esirkepov *et al.*, Phys. Rev. Lett., **89**,275002 (2002)
[5] G. Lehmann *et al.*, Phys. Plasmas, **13**,092302 (2006).
[6] S. V. Bulanov *et al.*, Phys. Fluids B, **4**,1935 (1992).
[7] Y. Sentoku *et al.*, Phys. Rev. Lett., **83**,3434 (1999).
[8] N. M. Naumova *et al.*, Phys. Rev. Lett., **87**,185004 (2001).
[9] S. V. Bulanov and F. Pegoraro, Phys. Rev. E, **65**,066405 (2002).
[10] M. A. Leontovich and S. M. Osovets, At. Energ., **3**,81 (1956); Ya. B. Zel'dovich and Yu. P. Raizer, *Physics of Shock Waves and High-Temperature Hydrodynamic Phenomena* (Academic Press, New York, 1967).
[11] L. D. Landau and L. M. Lifshits, *Electrodynamics of continuous media* (Pergamon, Oxford, 1984)..
[12] M. Borghesi *et al.*, Phys. Rev. Lett., **88**,135002 (2002).
[13] C. Hernandez-Gomez *et al.* RAL report no. RAL-TR-2008-025, p. 260, ISBN 978-0-9556616-4-8 (2008).
[14] G. Sarri *et al.*, New J. Phys. **12**,045006 (2010).
[15] M. Borghesi *et al.*, Phys. Rev. Lett. **92**,05503 (2004).
[16] J.F.Dempsey *et al.* Med. Phys. **27**,10 (2000).
[17] R.A. Fonseca, L.O. Silva, R.G. Hemker *et al.*, Lect. Not. Comp. Sci. **2331**,342 (2002).
[18] S. C. Wilks and W. L. Kruer, IEEE J. Quantum. Elect. **33**,1954 (1997).

Perspectives on radiative blast waves in laser-heated clustered gases

Contact *dan.symes@stfc.ac.uk*

D. R. Symes

Central Laser Facility, STFC, Rutherford Appleton Laboratory HSIC, Didcot, Oxon OX11 0QX, UK

M. Hohenberger, H. W. Doyle, S. Olsson Robbie and R. A. Smith

Laser Consortium, The Blackett Laboratory, Imperial College London, Prince Consort Road SW7 2BZ, UK

A.S. Moore, E. T. Gumbrell

Plasma Physics Division, AWE plc, Aldermaston, Reading RG7 4PR, UK

R. Rodríguez, J. M. Gil

Physics Department, University of Las Palmas de Gran Canaria, Las Palmas de Gran Canaria, Spain and Nuclear Fusion Institute-Denim, Polytechnic University of Madrid, Madrid, Spain

Introduction

The continuous growth in scale of laser systems has enabled the study of material behaviour under increasingly extreme conditions. In the 1990's this capability led to the inception of *laboratory astrophysics*, in which researchers perform well characterised experiments and use hydrodynamic scaling arguments to explain and predict what occurs in astrophysical phenomena[1-4]. The experiments also provide important data for *verification and validation* of various aspects of numerical codes such as atomic physics, equation of state, radiative transfer and hydrodynamics. Many of these investigations have been performed with very large facilities such as the Omega laser and the *Z* z-pinch because of the large laser energies or x-ray fluxes required to drive materials into regimes of interest. Laboratory astrophysics studies are core objectives for the NIF and HiPER fusion projects and could also be applied to Space Science projects. In this report we discuss an alternative method to create a high energy density environment which takes advantage of the remarkable absorption of short pulse laser light exhibited by clustered gases[5-7]. This allows us to conduct laboratory astrophysics experiments with smaller scale chirped pulse amplification lasers[5-18].

Regimes of radiative shock

One particular area of interest is that of *radiative shocks*, which are common in astrophysics. These cause complicated structures, such as those seen in supernova remnants, because the polytropic index is lowered through radiation and ionisation making the gas more compressible and so more susceptible to instabilities. For a strong shock the compression can be related to the polytropic index using the energy conservation jump condition to be $c = (\gamma + 1)/(\gamma - 1)$. This gives an ideal gas limit of c=4 for $\gamma = {}^5/_3$ and c=7 for $\gamma = {}^4/_3$, the value for a radiation dominated gas. In general, the calculation of a shock compression is more complicated because the terms for ionization and radiation energy flux in the jump condition cannot be ignored[19].

The ultimate goal for experiments is to drive shocks into the *radiation dominated regime* when the radiation energy density (or pressure) exceeds the thermal energy density (or pressure). More realistically the shocks fall into the *radiative flux regime* so that radiative effects are evident but the pressure is still dominated by the thermal contribution. This is shown in Fig. 1 where these thresholds are shown by the red and cyan lines[2]. For the shock to be affected the plasma must be optically thin to the radiation emitted by the shocked material and also the timescale for this loss must be faster than the time taken for convective heat transport. This gives us two additional limits in Fig. 1[1]: that the photon mean free path is larger than the scale size of the system (green), and that the radiative cooling time is shorter than the ratio of sound speed to scale size (blue).

These conditions are easily met in low density astrophysical environments such as supernova remnants[1], but it is challenging to reach such a regime in the laboratory. We show

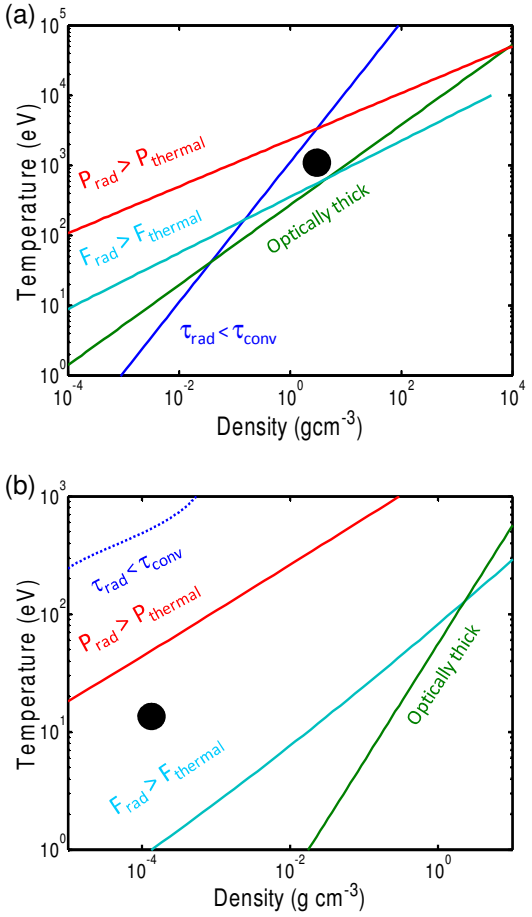

Figure 1. Plot representing the transitions between the various shock regimes described in the text. Cyan and red lines indicate the temperatures at which the radiative flux (F_{rad}) and pressure (P_{rad}) become dominant over the material quantities. Green and blue lines indicate when the photon mean free path is larger than the characteristic size of the system and the radiative cooling time (τ_{rad}) is shorter than the gas convection time (τ_{conv}) including only bremsstrahlung. In (b) the condition indicated by the dashed blue line is calculated using a radiative cooling function. The black circles mark the approximate properties of shocks created in (a) plastic and (b) clustered gases.

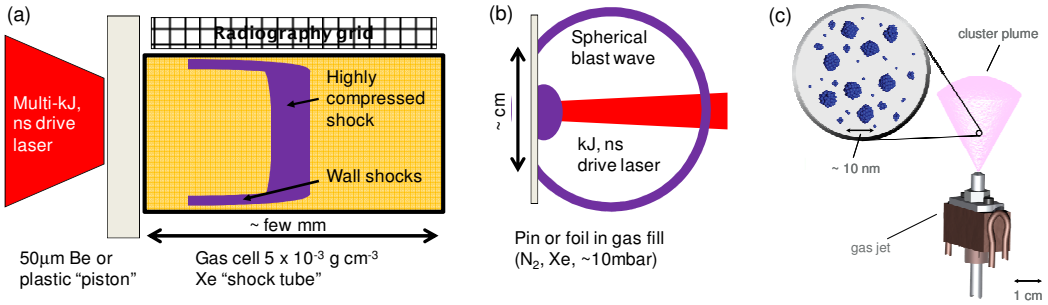

Figure 2. Methods to create radiative shocks (a) Piston driven shock, (b) solid target blast wave, (c) cluster blast wave.

this in Fig. 1(a) which corresponds to a typical experiment in a solid or foam target (represented by fully ionised carbon with a scale size h=100µm). Here we have followed the method of Ryutov *et al.*[1] and Drake[2] and used the blackbody expression for radiative flux and bremsstrahlung calculations for the radiation mean free path and cooling rate, which do not account for line radiation. The desired regime is tightly constrained and the high temperatures necessary mean that the shock speed must be very high (~100kms^{-1}). This is the reason that these experiments require kJ drive energies and correspondingly large laser systems. We can alleviate this requirement by launching shocks in gases. Because the density is so much lower (~10^{-4} gcm^{-3}), the shock speed needed to enter the radiative flux regime reduces to ~10kms^{-1}.

For the partially ionised gas, line radiation is the dominant energy transport mechanism meaning that the approximations used for the solid target are poor ones. To correctly categorize cluster shocks involves a complicated calculation of the radiative properties of the plasma considering line emission and without any assumption of equilibrium. We have recently started to apply the RAPCAL code[21] to the problem and the resulting calculation will be of great use to the laboratory astrophysics community. Until this is complete, we consider the plot shown in Fig. 1(b) for partially ionised xenon (Z^* = 0.63 $(T_{eV})^{½}$ [2]). The green, cyan and red lines are still calculated as in Fig. 1(a) so may not be accurate. For the blue line, we have used the (astrophysical) cooling rate from Post *et al.*[20] which is more appropriate than using the bremsstralung rate but may still be incorrect for the densities used in laboratory experiments. Nevertheless, the rapid cooling of the gas suggests that a wide range of densities and temperatures will fall into the radiative flux regime.

Creating radiative shocks

Three methods have been used to create radiative shocks in the laboratory (See Fig. 2). The first is to make a "shock tube"[22] by driving a solid density plastic or beryllium piston into a xenon gas cell. These experiments have been conducted at Omega[3,23] and LULI[3,24,25] using kJ lasers at a moderate intensity of ~10^{14} Wcm^{-2} in a large smooth focal spot (~500µm diameter) to create a planar geometry. Because the laser pulse is long (~ns) there is a continuous injection of energy to the shock, creating a *stationary* structure. Shock speeds are very high (>50kms^{-1}) and because of the strong radiative losses the shocked gas is highly compressed (c>30).

A different type of shock is created following a sudden release of energy in a zero-extension, instantaneous explosion. In this case, a shock moves into the surrounding medium sweeping up material into a thin dense shell called a *blast wave*. The shock decelerates and decays as it expands and, if the shocked material is hot, radiative losses cause the collapse of the shell to very high density and the onset of thin shell instabilities[26-29]. This is the situation encountered in supernova remnants, which are some of the most spectacular objects we observe. Radiative blast waves can be generated experimentally by using a kJ laser to irradiate a pin or foil within a moderate to high Z background gas[3,30,31]. The high laser energy is required to maintain a strong shock over relatively large spatial scales (~few mm). Alternatively the laser energy can be deposited directly into the gas to launch shocks[5-18,32,33]. Ordinarily a gas absorbs only a small fraction of the laser light, but if clusters form then the absorption is dramatically increased and a hot (T_e~keV), high energy density plasma (up to 10^8 Jcm^{-3}) is created. This plasma filament subsequently explodes into the ambient gas quickly forming a cylindrical blast wave[5]. In this way high Mach number shocks can be launched using high intensity (>10^{17} Wcm^{-2}) lasers with energies as low as 100mJ provided that the pulse duration is short enough to couple energy into clusters before they explode (sub-picosecond timescale).

Radiative shocks can be categorized according to the optical depth of the gas ahead of (upstream) and behind (downstream) the shock. This is important to determine the suitability of a laboratory experiment for astrophysical scaling[2] as shown in Fig. 3. Shocks in a supernova evolve from the top-right to the bottom-left of this plot. Initially, in the core of the supernova, both regions are optically thick. As the shock breaks out at the surface the precursor becomes optically thin and later, as the explosion forms a supernova remnant, the postshock region also becomes optically thin. The Omega and LULI experiments performed with solid density pistons fall into the 'thick-thin' regime. The low density gas blast wave experiments are expected to be 'thin-thin', although Drake suggests that because of the large volume of gas ahead of the shock, these conditions could actually be 'thin-thick'. From our calculations we estimate the photon mean free path to be very similar to the scale size of the cluster blast waves so this differentiation is not so well defined.

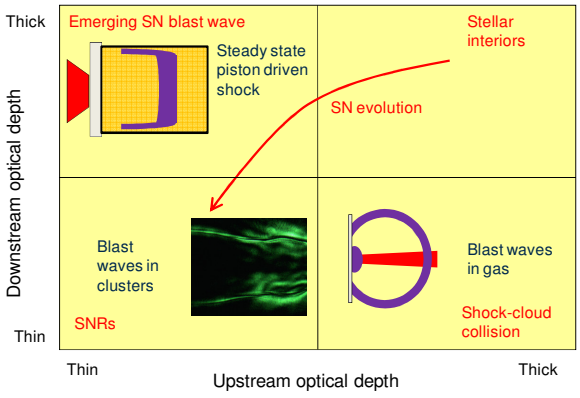

Figure 3. Categorising radiative shocks by upstream and downstream optical depth. Adapted from Ref. 2.

Characterising cluster blast waves

In order to assess the suitability of cluster shocks for scaling to astrophysical conditions we must be able to accurately define our experimental conditions. We have previously made some estimates of the plasma properties[13] and here we further consider the morphology of our blast waves. The structure of a typical blast wave launched in xenon clusters with a laser energy of 350mJ is shown in Fig. 4. This is taken at 17ns when the material has been swept up into a thin shell behind a steep shock front. Ahead of this, a large precursor with a peak electron density about half of the post-shock value extends almost 1000μm into the ambient gas. This precursor is less prominent with lower laser energies and lower gas densities. Additionally, when the gas density is decreased the shock decelerates more quickly and the thickness of the shock shell is reduced. These three effects are consistent with a lowering of the opacity of the gas, meaning that less energy is deposited in the precursor and there is a higher energy loss from the system. A measurement of the shock front trajectory in low density xenon (radius ~ $t^{0.39}$) suggests that the blast waves are fully radiative i.e. 100% of the incoming kinetic energy is radiated away[10].

From the electron density measurement shown in Fig. 4, we can attain some properties of the plasma. The ambient density in this case was ρ = 0.25 kgm^{-3} (10^{18} atoms cm^{-3}) so in the precursor we have a direct measurement of the average ionization <Z>~6. From the shell thickness, and assuming all the material lies within this shell, we obtain a compression of ~2. Using the postshock electron density of 14 x 10^{18} cm^{-3} we find that the postshock <Z> is similar at ~6. If we assume that the plasma is in local thermal equilibrium (LTE) we can then estimate the pre- and post-shock temperature using <Z> and ρ to be ~8eV. The constant temperature across the shock front implies that we have driven a shock in the *supercritical* (SC) regime. This is feasible since the threshold velocity for a SC shock at this relatively low density is ~7kms^{-1} [34], less than our measured shock velocity of ~10kms^{-1}. Further evidence comes from the shape of the precursor on some of our shots which have a plateau in the electron density profile which is commonly associated with SC shock formation. However, the assumption of LTE is a poor one since the plasma is not optically thick to the radiation.

The low compression we observe is a consequence of the high temperature of the precursor, which results in the pre-shock Mach number being drastically reduced (M~1.6) and so negating the strong shock approximation. In fact a calculation of the compression is further complicated because the gas is partially ionized, affecting the polytropic index. The energy conservation jump condition across the shock can be generalized to take into account both the ionization and the radiation flux[19]. However, the calculation of these fluxes is very complicated because the plasma is non-LTE and dominated by line emission. In addition, energy is not necessarily conserved across the shock because both pre- and post shock regions radiate energy in all directions.

To address these issues sophisticated numerical codes are necessary. There has been some success comparing experimental data to simulation results from hydrocodes which use the LTE approximation[8-10,17]. Edwards *et al.*[9] matched the trajectory of a xenon blast wave and identified the switch between a *radiative phase*, lasting from shock formation until several tens of nanoseconds, and an *energy recovery phase* when the blast wave sweeps up energy it has previously deposited in the precursor. We have observed this transition, at about the same time in the shock evolution, in several experiments since then[17]. We find reasonable agreement of simulation results with the shock shell electron density profile (Fig 4(a), Ref. 17) but the code overestimates the length of the precursor. Keilty *et al.*[10] compared the radiative cooling rates given by a non-LTE calculation by Post *et al.*[20] and those given by the LTE HYADES hydrocode[35] and found a large discrepancy for xenon. This highlights the need for a non-LTE approach to the simulations but as yet we have been unable to apply non-LTE versions of the hydrocodes.

Recently we have started investigations using the RAPCAL code[21]. This code can calculate radiative properties for optically thin and thick plasmas for both low and high Z over a wide range of density and temperature. This will enable us to more accurately determine gas opacities and radiative cooling rates without the assumption of LTE. Initial calculations were performed for a xenon plasma at a density of 2 x 10^{-4} gcm^{-3} and a temperature of 10eV which is similar to our experimental conditions. From Table 1 it would appear that the plasma is in LTE, but this is a consequence of using the LTE temperature value as an initial condition, which is a crude approximation. We are currently working to resolve this by using direct measurements to create the inputs for simulations.

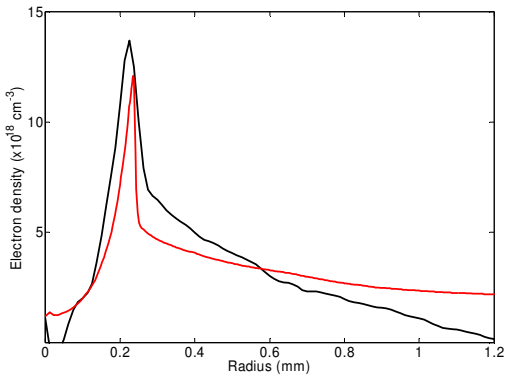

Figure 4. Electron density profiles measured in cluster blast waves at 17ns with a simulation using the NYM code (red).

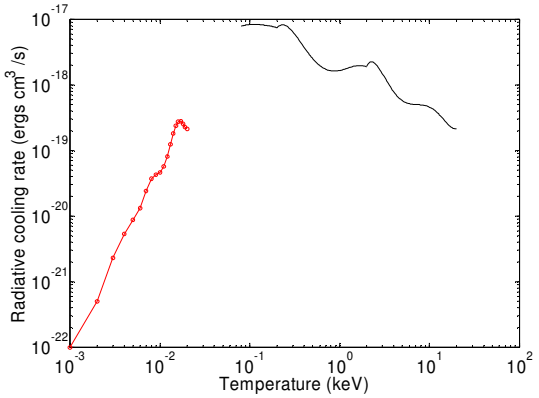

Figure 5. Radiative cooling rate for xenon calculated using RAPCAL (1 – 20eV) and the cooling rates from Ref. 20 (80 – 2000eV). The radiative power loss (ergs cm^{-3}s^{-1}) is obtained by multiplying the cooling rate by <Z>n_i^2.

With this caveat in mind, we draw some conclusions from the values in Table 1. Immediately clear is that the radiative emission is completely dominated by line emission (bound-bound). Therefore, any use of the bremsstrahlung cooling rates used by Ryutov *et al.*[1] or a blackbody treatment of radiative flux[19] is wholly inappropriate. It also highlights the need for temporally and spatially resolved line emission measurements in future experiments. The radiative cooling time is extremely short so fulfils the condition of being shorter than convective timescales. However, the photon mean free path using the Planck mean opacity is ~100μm, similar to the scale of the shell

thickness and the precursor length, so the plasma cannot clearly be identified as either optically thin or thick. We also compare (per unit length) the radiated power loss to the kinetic energy entering the blast wave per unit time[10] and find values of 3 x 10^9 $Jm^{-1}s^{-1}$ and 2 x 10^8 $Jm^{-1}s^{-1}$ respectively. This agrees with our experimental conclusion that the blast waves are fully radiative. In fact, the radiative flux is larger than the kinetic flux, possible in a blast wave because there is an initial energy provided in the explosion.

Shock instabilities

One of the main motivations for launching strongly radiative blast waves in xenon clusters is to drive a collapse of the shell and so spontaneously trigger shock instabilities. The first experiments at the Lawrence Livermore National Laboratory hoped to observe the Vishniac overstability[26,27] which causes oscillating ripples on the shock front and is thought to be the origin of complex structure in supernova remnants. In fact the shock shell collapse was prevented by electron heat conduction thickening the shell and also heating of the precursor lowering the strength of the shock. Furthermore, in a theoretical study[29] Laming showed a threshold velocity for the Vishniac overstability in xenon to be 25kms^{-1}, higher than that attained in the Livermore experiment. This is somewhat of a catch-22 since to drive stronger shocks requires higher laser energies but this leads to more preheat which prevents high compression. In our recent campaign using Vulcan TAW we did see shock compressions which exceeded the non-radiative limit (c=4)[36] but were probably still insufficient for the shock to be unstable to the Vishniac mechanism. The solution may be to lower the density of the target so that the gas is less opaque to the radiation. We already have evidence[17] that this leads to higher energy loss and higher shell compression while reducing the size of the precursor.

Another instability associated with thin shell blast waves is the thermal cooling instability (TCI)[28]. This arises when a shock enters a cycle of stall and recovery as it repeatedly loses energy through radiative losses but then rebuilds as it sweeps up the hot preshock gas. In astrophysical shocks unstable to the TCI it is predicted that the shock velocity will oscillate as it decays with a timescale of order 1000 years. To recreate this situation in the laboratory we must have energy exchange between the shocked material and its precursor. So the higher density cluster blast waves with very prominent precursors are ideal and the observation of an energy recovery phase indicates that the first stage of the process occurs even when we use low energy drive lasers (~100mJ)[9]. With the high drive energies used in the Vulcan TAW experiment, we measured full trajectories on a single shot[16] and observed oscillations which we attribute to this mechanism. For the TCI to occur, the cooling rate of the gas must be falling as the temperature increases (the cooling function $\Lambda(T) \propto T^{\beta}$ has an exponent $\beta<1$). The radiative cooling rate for xenon is plotted against temperature in Fig. 5. The values up to 20eV are from a RAPCAL calculation and those above 80eV were obtained using the method of Post *et al*.[20]. For astrophysical conditions, β is commonly less than 1 but in the laboratory this is more difficult to achieve. This calculation suggests that if we could drive xenon blast waves to temperatures above 17eV then $\beta < 1$. The observation of the velocity instability on Vulcan was in krypton and these cooling rates are currently being calculated.

		NLTE	LTE
<Z>		6.627	6.734
Fractional population of most abundant ions	Xe VII	0.356	0.312
	Xe VIII	0.518	0.529
	Xe IX	0.079	0.121
Rosseland mean opacity (cm^2/g)		1.987e3	
Planck mean opacity (cm^2/g)		1.27e5	
Radiative power loss ($erg\,cm^{-3}s^{-1}$)	Bound-bound	5.61e17	8.86e17
	Bound-free	4.32e13	-
	Free-free	1.20e14	-
	Total	5.61e17	8.86e17

Table 1. Calculations of radiative properties using the RAPCAL code

Conclusions

Since the potential of clustered gases for laboratory astrophysics experiments was recognized[8], we have explored avenues to exploit the versatility of the method. We have demonstrated techniques which are relatively simple to perform in clusters for single-shot trajectory measurements[16,36], creating shock collisions[12,15], imprinting periodic shock front modulations [15,18] and controlled pre-ionization of the upstream gas[7]. Spatial shock front instabilities are difficult to initiate in cluster blast waves because of low compression[9] but we have measured a velocity oscillation in krypton blast waves launched with high laser energy[36]. Unlike the Vishniac overstability, the velocity instability cannot be studied using the stationary shock piston approach as it involves a decaying shock.

We have made progress in understanding the plasma conditions in the cluster blast waves. The system is complicated because it is not in equilibrium and cannot easily be classified as either optically thin or thick. We therefore have employed the RAPCAL atomic physics code which does not rely on these approximations. Ideally this will be coupled to simulations with non-LTE, multi-dimensional radiation-hydrocodes but this presents a difficult challenge.

References

1. D. Ryutov, R. P. Drake, J. Kane *et al*., *Astrophys. J.* **518**, 821 (1999).
2. R. P. Drake, *High Energy Density Physics: Fundamentals, Inertial Fusion, and Experimental Astrophysics* (Springer, 2006), 1st ed.
3. B. A. Remington, R. P. Drake and D. D. Ryutov, *Rev. Mod. Phys.* **78**, 755 (2006).
4. R. P. Drake, *Physics Today*, p. 28, June 2010
5. T. Ditmire, K. Shigemori, B. A. Remington *et al*., *Astrophys. J. Suppl. Ser*. **127**, 299 (2000).
6. E. T. Gumbrell, A. S. Moore, J. A. Lazarus *et al*., *New J. Phys.* **10**, 123011 (2008).
7. M. Hohenberger *et al*., CLF Annual Report, p. 23, 2007/2008
8. K. Shigemori, T. Ditmire, B. A. Remington *et al*., *Astrophys. J. Lett*. **533**, L159 (2000).
9. M. J. Edwards, A. J. MacKinnon, J. Zweiback *et al*., *Phys. Rev. Lett.* **87**, 085004 (2001).
10. K. A. Keilty, E. P. Liang, T. Ditmire *et al*., *Astrophys. J.* **538**, 645 (2000).
11. A. S. Moore, D. R. Symes, and R. A. Smith, Phys. Plasmas **12**, 052707 (2005).
12. D. R. Symes, J. Osterhoff, R. Faustlin *et al*., *High Energy Density Physics* **3**, 353 (2007).
13. A. S. Moore, J. Lazarus M. Hohenberger *et al*., *Astrophys. Space Sci.* **307**, 139 (2007).

14. R. A. Smith, J. Lazarus, M. Hohenberger *et al*., *Astrophys. Space Sci.* **307**, 131 (2007).

15. R. A. Smith, J. Lazarus, M. Hohenberger *et al*., *Plasma Phys. Control. Fusion* **49**, B117 (2007).

16. A. S. Moore, E. T. Gumbrell, J. Lazarus *et al*., *Phys. Rev. Lett.* **100**, 055001 (2008).

17. J. Osterhoff, D. R. Symes, A. D. Edens *et al*., *New J. Phys.* **11**, 023022 (2009).

18. D. R. Symes, M. Hohenberger, J. Lazarus *et al*., *High Energy Density Physics* **6**, 274 (2010).

19. C. Michaut, C. Stehlé, S. Leygnac *et al*., *Eur. Phys. J.* D **28**, 381 (2004).

20. D. E. Post, R. V. Jensen, C. B. Tarter, *et al*., *At. Data Nucl. Data Tables* **20**, 397 (1977).

21. R. Rodriguez *et al*., *Laser and Particle Beams* **26**, 433 (2008).

22. M. Busqeut *et al*., *Rev. Sci. Instrum.* **81**, 023502 (2010).

23. A. B. Reighard, R. P. Drake, K. K. Dannenberg *et al*., *Phys. Plasmas* **13**, 082901 (2006).

24. S. Bouquet, C. Stehlé, M. Koenig *et al*., *Phys. Rev. Lett.* **92**, 225001 (2004).

25. M. Koenig *et al*., *Phys. Plasmas* **13**, 056504 (2006).

26. E. Vishniac, *Astrophys. J*. **274**, 152 (1983); D. Ryu and E. T. Vishniac, *ibid.* **313**, 820 (1987); **368**, 411 (1991).

27. J. Blondin *et al*., *Astrophys. J.* **500**, 342 (1998).

28. P. A. Kimoto and D. Chernoff, *Astrophys. J.* **485**, 274 (1997).

29. J. M. Laming and J. Grun, *Phys. Plasmas* **10**, 1614 (2003).

30. J. Grun, J. Stamper, C. Manka *et al*., *Phys. Rev. Lett*. **66**, 2738 (1991).

31. A. D. Edens, T. Ditmire, J. F. Hansen *et al*., *Phys. Rev. Lett.* **95**, 244503 (2005).

32. T. R. Clark and H. M. Milchberg, *Phys. Rev. Lett.* **78**, 2373 (1997).

33. P. M. Nilson, S. P. D. Mangles, L. Willingale *et al*., *Phys. Rev. Lett.* **103**, 255001 (2009).

34. M. Gonzales, E. Audit and C. Stehle, *Astronomy & Astrophysics* **497**, 27 (2009).

35. J. T. Larson and S. M. Lane, *J. Quant. Spectrosc. Radiat. Transfer* **51**, 179 (1994).

36. M. Hohenberger, submitted to *Phys. Rev. Lett*. (2010).